MODELING OF MECHANICAL AND HYDRAULIC PROPERTIES OF STRUCTURED GEOMATERIALS

MODELING OF MECHANICAL AND HYDRAULIC PROPERTIES OF STRUCTURED GEOMATERIALS

By POUNEH PAKDEL, B.Sc., M.Sc.

A Thesis Submitted to the School of Graduate Studies in Partial Fulfilment of the Requirements for the Degree Doctor of Philosophy

McMaster University DOCTOR OF PHILOSOPHY (2025) Hamilton, Ontario

(Civil Engineering)

TITLE: Modeling of Mechanical and Hydraulic Properties of Structured Geomaterials

AUTHOR: Pouneh Pakdel, B.Sc., M.Sc. (Guilan University)

SUPERVISOR: Professors S. Pietruszczak

NUMBER OF PAGES: x, 88

ABSTRACT

The thesis involves studies of the mechanical and hydraulic behaviour of rock formations used in various geotechnical applications, including underground development, resource extraction, and nuclear waste management. The mechanical response of Cobourg limestone is investigated first. This rock is inherently anisotropic due to stratification as well as the heterogeneity of its fabric, which consists of light grey nodular carbonates and darker argillaceous partings. In this work, a fabric-dependent approach is developed to describe the strength and deformation characteristics of this rock. The study demonstrates that Cobourg limestone can be modeled as a transversely isotropic material by invoking stereological principles and the notion of mean intercept length as a fabric descriptor. The mechanical response is influenced by the spatial variability of argillaceous partings, making the concept of Representative Elementary Volume (REV) inapplicable in most cases. A series of numerical simulations of triaxial tests conducted on differently oriented samples is performed, which highlights the impact of fabric heterogeneity on the mechanical behavior.

In addition to studying the mechanical properties of Cobourg limestone, this thesis also addresses the assessment of hydraulic conductivity of sparsely fractured rock masses. Simplified methodologies, such as Oda's permeability tensor and pipe network models, are compared with a more advanced approach incorporating a constitutive law with embedded discontinuity (CLED). Several numerical examples are provided, examining the fluid flow in discrete fracture networks. The study compares the estimates of principal values and directions of equivalent permeability tensor for different models. Results indicate that the pipe network model, enhanced by an algorithm from graph theory, provides predictions consistent with the CLED approach, particularly for the orientation of principal permeability directions. A pragmatic approach is then proposed on the basis of these findings for the definition of the anisotropic equivalent hydraulic conductivity operator in fractured rock masses.

ACKNOWLEDGEMENTS

I will be eternally grateful to my supervisor, Dr. Stanislaw Pietruszczak, who provided me with exceptional guidance, enthusiastic encouragement, and priceless knowledge during the pursuit of this research. His patience and insight have been the most imperative in the shaping of my academic career. In addition, I sincerely appreciate the insightful feedback and guidance from my supervisory committee members, Dr. Peijun Guo and Dr. SeonHong Na, during our annual meetings. Their comments and suggestions have been instrumental in refining my research. I also want to express my deepest sense of gratitude to Dr. Mehdi Veiskarami who introduced me to geomechanical studies and provided me with his support and advice.

I would like to express my deepest gratitude to Amir Arsalan Jameei, Hojjat Mohammadi, Ehsan Benabbas, and Kianoosh Koocheki for their extensive support and valuable comments and for the moral support that has never stopped during this PhD journey. Lastly, I am very much grateful to my family for their unconditional love, support, and belief in me.

TABLE OF CONTENTS

LIST OF ILLUSTRATIONS

LIST OF TABLES

CHAPTER 1

Introduction

1.1 Problem Statement

Anisotropy in rocks arises from the alignment of minerals or the presence of layered structures, fractures, and partings. This makes predicting the mechanical behavior of these rocks more complex than that of isotropic materials. The Cobourg limestone, which is examined in this work, has a heterogeneous fabric characterized by the presence of argillaceous inclusions of different volume fractions. The presence of these partings, which are weaker than the surrounding carbonate matrix, introduces variability in the strength and stiffness properties, which depend on the orientation of loading. The ability to predict the mechanical anisotropy is crucial for the safe design of structures interacting with this and other similar sedimentary formations.

A meaningful understanding of the mechanical behavior of Cobourg limestone entails a detailed study of the influence of fabric on the strength and deformation characteristics. In this chapter, an effort is made to quantify the heterogeneity of fabric on the basis of stereological principles wherein the mean intercept length (MIL) is utilized as the primary descriptor. The chapter lays out a framework to correlate the fabric parameters with strength anisotropy by invoking the notion of a fabric tensor. The results of triaxial tests are examined to assess the impact of argillaceous partings on the mechanical behavior.

1.1.1 Mechanical Anisotropy of Cobourg Limestone: Challenges and Approaches

Cobourg limestone is a sedimentary rock formation in Ontario dating back to Ordovician period. This geological formation has been considered as a host rock for a potential low and intermediate level waste Deep Geologic Repository (DGR) at the Bruce nuclear site at Kincardine. The rock has high strength, low permeability and high sorption capacity so it would constitute an efficient barrier to radionuclide migration. The Cobourg limestone is inherently anisotropic and heterogeneous (cf. [1, 2]). Anisotropy is due to stratification resulting from the sedimentation process; heterogeneity, on the other hand, originates from the interspersed fabric (cf. [3, 4]).

The fabric of the Cobourg limestone consists of a fine-grained light grey nodular fraction separated by a darker limestone containing the clay minerals, the latter referred to as argillaceous partings (cf. [5, 6]). The heterogeneous nature of this limestone is visible even at the macroscale. The rock's matrix includes carbonate, clay, and fossiliferous material, with individual components ranging in size from 2 mm to 8 mm. The light gray nodules, which form the dominant component, range in diameter from 10 mm to 50 mm and are separated by darker clay-rich partings. Fig. 1-1 shows pictures of cylindrical samples of Cobourg limestone cored along and perpendicular to the planes of nominal stratification (after [4]). The overall assessment of fabric can be made based on observation of the exposed surfaces. However, a more accurate evaluation involves invasive and non-invasive (e.g. CT imaging) methods of mapping the interior of the samples.

Fig. 1-1. Heterogenous fabric in samples of Cobourg Limestone; light grey limestone and argillaceous parting (after ref. [7])

The mineral composition significantly influences the mechanical properties of Cobourg limestone. More than 90% of the light gray nodular fraction consists of carbonate minerals, primarily calcite and dolomite. Additionally, quartz forms approximately 8%, with 0.3% consisting of trace clay minerals. In comparison, the darker argillaceous partings contain carbonates with 66% calcite and dolomite, 22% quartz and have a clay content of 2.4%, which includes illite, kaolinite, and traces of montmorillonite. Table 1-1. provides details of mineralogical composition. The average porosity of the Cobourg Limestone is approx. 0.9%, which indicates that there is a very limited void space within the rock matrix, and the average dry density is around 2.33 g/cm3 (ref. [8]).

Table 1-1. Mineralogical composition of the Cobourg limestone (after ref. [9])

Light grey		Dark grey	
Minerals	%	Minerals	%
Quartz	8.01	Quartz	22.00±5.9
Calcite	85.4	Calcite	51.45±13.3

Dolomite	5.3	Dolomite	15.85±6.6
Albite	0.73	Albite	3.25±1.1
Mocrocline	0.25	Mocrocline	3±0.2
Muscovite	0.16	Muscovite	1.55±0.9
Chlorite	0.13	Chlorite	0.80±0.3
Pyrite	0.08	Pyrite	1.45±0.8
Haematite	0.03	Haematite	0.65±0.2

As mentioned before, Cobourg Limestone's microstructure reflects the geologic processes of deposition with varying environmental conditions, which led to formation of distinct layers with contrasting properties. The presence of partings contributes towards the overall deformation and strength properties of this rock, as the partings are mechanically weaker than the surrounding carbonate material. Hence, the failure mechanism, deformability, and overall rock mass stability are all affected by the volume fraction and the orientation of these partings with respect to the loading direction.

The mechanical properties of Cobourg limestone have been investigated quite extensively. The experimental work involved a range of standard tests, which included unconfined compression, indirect tension and triaxial compression, as well as hydraulic pulse tests to estimate the permeability (cf. [8, 9, 10]). In addition, several studies were conducted examining the effects of temperature, partial saturation as well as the time-dependence (e.g. [11, 12, 13]).

In ref. [14], Ghazvinian and co-authors reported the results of an investigation focused on the effects of anisotropy of strength. The testing program involved uniaxial compression, triaxial and indirect tensile (Brazilian) tests. Large diameter cores, which were obtained from a quarry in Bowmanville (Ontario), were drilled in five different orientations with respect to the direction of stratification, i.e. at 0, 30, 45, 60 and 90 degrees. For each orientation, 6 specimens were prepared and tested for UCS. Triaxial tests were also completed for each orientation set and included specimens tested at different confining pressures.

Fig. 1-2 shows the distribution of uniaxial compressive strength in samples tested at different orientations. The scatter in the experimental data, which likely stems from fabric heterogeneity, is considerable; at the same time, however, there is strong evidence of anisotropy. The mean value of strength for vertical and horizontal samples is approximately 60 MPa and 90 MPa, respectively.

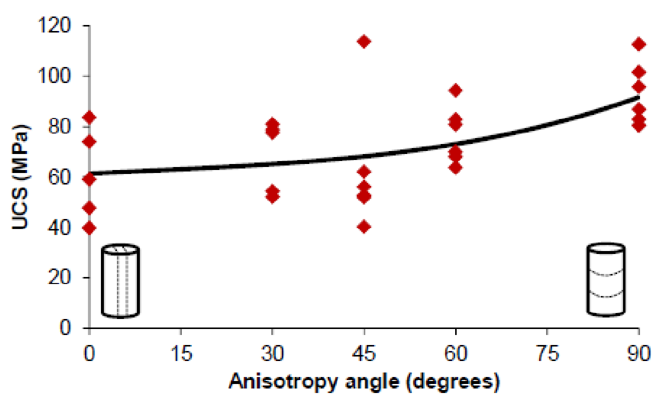

Fig. 1-2. Uniaxial compressive strength (UCS) for different orientations of specimens (after ref. [14])

The specimens for triaxial testing were prepared based on the same specifications as those used for the UCS specimens. During the tests, the axial and lateral displacements were recorded using LVDTS and a chain extensometer wrapped around the specimen circumference, respectively. The tests were carried out at confinements of 4 MPa and 10 MPa. The data collected from UCS and triaxial tests for the Cobourg limestone specimens with different fabric orientations were used to establish the Hoek-Brown failure envelopes. No details on the specification of material parameters and/or the accuracy of this representation have been provided in ref. [14]. The results, however, clearly indicate that the conditions at failure are strongly affected by the sample orientation (Fig. 1-3).

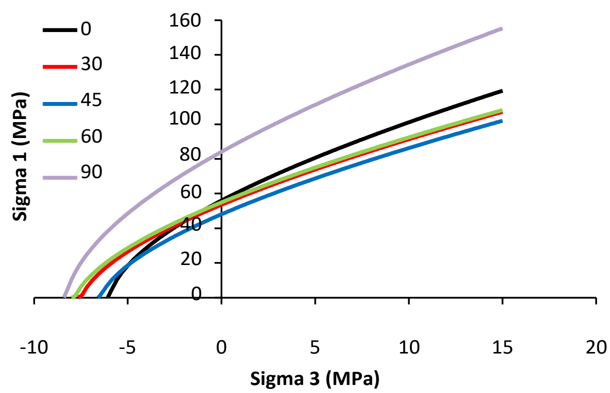

Fig. 1-3. Hoek-Brown envelopes of different fabric orientations (after ref. [14])

In another independent study published in an NWMO report [10], Selvadurai reported the results of an extensive laboratory investigation on Cobourg limestone conducted at McGill University. The rock specimens were collected again from the Saint Mary's Quarry at Bowmanville in Ontario. The specimens were selected based on the visibility of stratification. The tests were performed on samples cored along, perpendicular to and at inclinations of 45^0 and 30^0 to argillaceous partings, which were assumed to be aligned along the nominal stratification. The experimental program included the assessment of uniaxial compressive strength and tensile strength using both Brazilian tests and a newly developed plug compression test, as well as a series of triaxial tests conducted in Obert-Hoek cell to provide estimates for the deformability and strength characteristics.

The key results of unconfined compression tests and the Brazilian indirect tension tests are provided in Tables 1-2 and 1-3. It is evident that for samples cored at the same orientation relative to stratification, the scatter in the experimental data is quite significant. This, again, can be attributed to the fact that the volume fraction of constituents and their distribution is likely to be different in each sample. It is worth noting that in the original report, the authors also examined the size dependency of the compressive strength. They demonstrated that the average values remained within a wide range of 70-130 MPa with a significant standard deviation. Given this information, it is difficult to draw any quantitative conclusions regarding the presence and/or the nature of anisotropy.

Table 1-2. Results of uniaxial compression tests on samples normal (H) and parallel (V) to argillaceous partings (after ref. [10])

Sample	UCS (MPa)	Young Modulus (GPa)
HA7	88.2	21.2
HA33	103.5	22.3
HA34	104.0	22.3

Sample	UCS (MPa)	Young Modulus (GPa)
V13	56.9	22.1
V14	116.6	27.7
VC3	88.2	21.2
VC9	118.3	30.0

Table 1-3. Results of Brazilian tension testing (after ref. [10])

Sample	Tensile Strength (MPa)	Sample	Tensile Strength (MPa)	Sample	Tensile Strength (MPa)
HA6	7.30	VB6	9.70	VB5	6.90
HA21	8.50	VB12	2.90	VB13	6.90
HA21	9.60	VC11	7.10	VC6	6.85
HB33	6.20	VC17	6.90	VC7	11.0

In the opinion of authors of the NWMO report, the testing program demonstrated that the strength characteristics of the Cobourg limestone might be perceived as largely isotropic and the argillaceous partings, although visibly distinct in their orientations, do not contribute to the generation of any strength anisotropy. Thus, '…based on the results of experiments, the strength and deformability characteristics of the Cobourg limestone can be represented by equivalent values applicable to an isotropic model'. The validity of these conclusions, however, may be questioned.

For the triaxial tests in Obert-Hoek cell tests, the orientation of samples was restricted to the cores aligned either along or normal to the argillaceous partings. The tests were performed at confinement within the range from 5 MPa to 60 MPa. The detailed results of all triaxial tests are provided in the original report. The primary conclusion emerging from these results was that the conditions at failure may be represented by Mohr-Coulomb criterion with a cut-off in tension regime. The failure envelopes are presented in Fig. 1-4. The linear approximation indeed appears to be quite accurate. Also, there is no visible difference in the values of strength parameters for samples tested along and perpendicular to argillaceous partings, indicating that the effects of anisotropy are not significant. Given the earlier comments, however, the latter conclusion may be questioned.

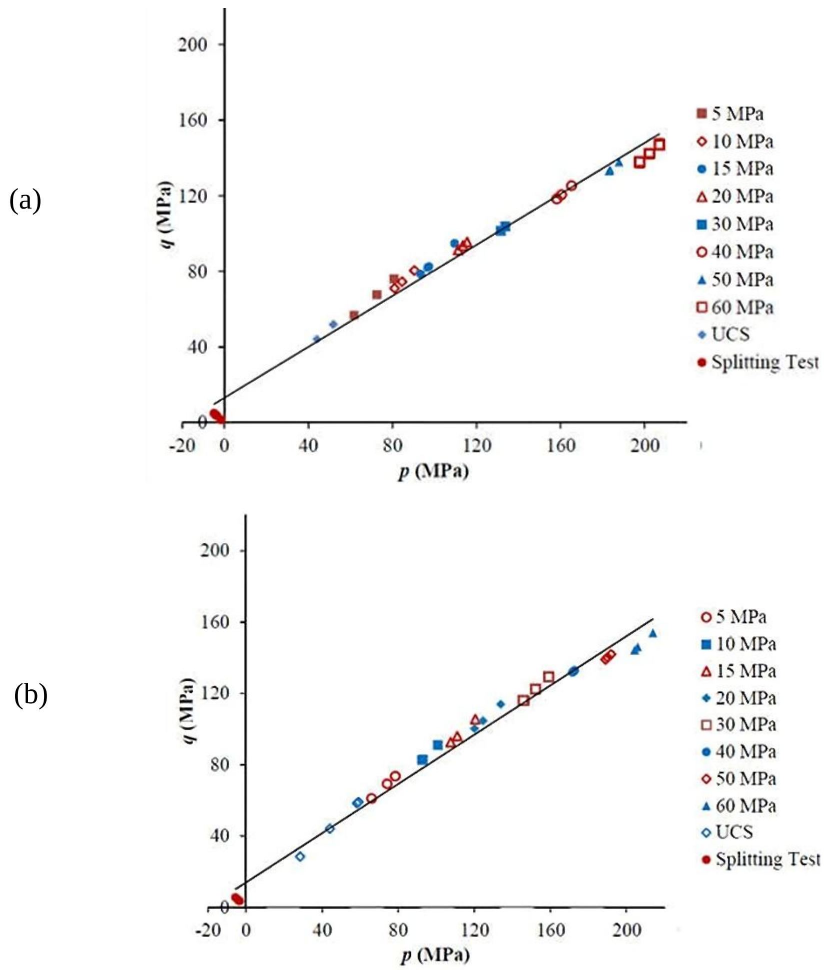

Fig. 1-4. Results of triaxial test conducted using the Obert-Hoek Cell; specimens aligned (a) normal to and (b) along the argillaceous partings (after ref. [10])

A major factor in determining the properties of Cobourg limestone is the selection of the sample size, which may be perceived as the Representative Elementary Volume (REV). This, in turn, requires information on sample fabric and its quantification by some measure of heterogeneity of microstructure. Unfortunately, in the tests on Cobourg limestone conducted so far, the mechanical response was not explicitly correlated with the sample's fabric. Therefore, it is difficult to interpret the tests results and draw any quantitative conclusions in relation to anisotropy in strength and stiffness properties. It seems that for Cobourg limestone, the notion of REV may not, in general, be applicable as the effects of size are explicitly linked with heterogeneity, which varies among samples of different dimensions.

Alongside the experimental work, some research has also been conducted on the implementation of various constitutive models for Cobourg limestone. Both the discrete and continuous frameworks have been employed. The former are based on the distinct-element method that perceives the material as an assembly of non-uniformly-sized circular or spherical particles that are joint together at their contact points [15]. An example of this approach is the Synthetic Rock Mass (SRM) model (cf. refs. [16–17]). The latter has been used to simulate the fracturing of intact rock across different scales, including studies related to the Excavation Damaged Zone (EDZ) (cf. refs. [18–19]). It should be pointed out, however, that there are several issues with the SRM approach. First, it requires a detailed information about the contact properties between particles. These properties, however, cannot be determined from any experimental test. Furthermore, the description of rock mass as a collection of bonded particles is not very realistic, and their shape, size and number are quite speculative. Thus, this approach may provide information on the deformation mechanism at the mesoscale, but it will not yield accurate quantitative predictions for larger-scale applications.

The continuum analysis employed the so-called *damage initiation and spalling limit* [20] model and the *cohesion-weakening friction-strengthening* model [21]. The former approach is an empirical predictive technique, which does not provide any consistent mathematical framework for modeling the onset and propagation of localized damage. At the same time, the cohesion-weakening approach is also questionable as it attributes the strain-softening effects to material behaviour (viz. reduction in cohesion). In this case, the material properties are size-dependent and cannot be uniquely defined. Also, the finite element solution is strongly affected by the discretization of the domain.

1.1.2 Assessment of equivalent permeability tensor in sparsely fractured rock masses

The second part of this research shifts its focus to crystalline rocks, with a particular emphasis on fluid flow through rock masses containing fractures. Fractures exist in most geologic structures, but in crystalline rocks they occur with particular frequency and have a major influence on both mechanical and hydraulic properties. Unlike Cobourg limestone, where the main concern is mechanical anisotropy, crystalline rocks are primarily studied for their hydraulic properties, especially in cases where the existing fracture networks control fluid flow. Although fractures occupy a small proportion of rock mass, they play a significant role in terms of permeability, creating high-conductivity channels for fluids through them. This is particularly important in hard rock environments, where the intact rock has extremely low permeability, making fractures the primary paths for fluid movement.

Understanding the hydraulic behavior of fractured rock mass is important for many rock engineering's operations, such as petroleum production, groundwater storage, geothermal energy production, and nuclear waste management [22,23,24]. In view of this, a significant amount of research has been focused on estimating the effective permeability of rock masses with randomly distributed fractures (see refs. [25-27]). The flow of fluid through fractured rock masses is predominantly controlled by the geometry of the fracture network. This includes orientation, spacing, and connectivity of fractures. Interconnected fractures make effective flow channels, whereas isolated or discontinuous fractures restrict fluid movement and reduce the overall volume of flow.

One of the most common representations of permeability (or hydraulic conductivity) of fractured rock is that of a symmetric second order tensor [28,29]. The equivalent permeability tensor is, in general, scale-dependent in character, as its eigenvalues and eigenvectors depend on a spatial distribution of fractures [30]. Experimental studies (e.g., refs. [31,32]) and numerical studies with Discrete Fracture Network (DFN) models (e.g., refs. [33,34]) have both confirmed that, with a variation in observation scales, permeability can vary appreciatively. These studies illustrate the demand for efficient modeling techniques capable of describing complex, scale-dependent behavior of fluid flow in fractured rock masses.

A second significant factor in controlling permeability in fractured rocks is fracture aperture, which directly affects hydraulic conductivity. Fracture aperture is not a property but a dynamic variable and changes in response to the state of stress in the rock mass. Stress changes cause fractures to dilate, close, or displace through shear movement, all of which impact permeability and the way in which fluids are able to flow through the rock [35].

Fluid flow in discrete fracture networks is generally analyzed with one of two dominant approaches: the macroscale model or the mesoscale model. In the mesoscale model, individual fractures are considered to act as principal channels for fluid flow, with each individual fracture explicitly modelled in terms of its geometry. The mesoscale analysis often tends to employ coupled hydromechanical simulations, taking into consideration the impact of changing stress field on the fractures' aperture. In this case, a high accuracy in terms of predicting the flow pattern can be achieved. That accuracy, however, comes at a price, as substantial computational effort is required that is associated with the need for fine discretization. The latter typically employs interface elements (e.g., ref. [36]) or requires additional degrees of freedom, as in the case of the Extended Finite Element Method (XFEM) [37]. Consequently, such a model can become computationally costly and not feasible for use in a large-scale problem. Additionally, numerical instabilities can arise due to a stark contrast between the hydraulic and geometric properties of fractures and the surrounding intact rock matrix, further complicating the implementation of this approach [38].

The macroscale models approximate the local interactions using various techniques, such as the dual permeability model, the multiple interacting continua approach, etc. (cf. refs. [39-41]). Instead of considering every fracture explicitly, the macroscale methods assess the equivalent permeability through upscaling techniques. This is done using analytical approximations or flow-based averaging techniques, such as boundary integration and volume averaging. Detailed reviews of different methodologies can be found in refs. [42,43].

Oda's permeability tensor approach [44,45] is one of the most common analytical techniques for estimating the permeability of fractured rock masses. This model employs the key geometric properties of the fracture network, such as fracture aperture, orientation, and size, and represents them using a second-order symmetric "crack tensor". The principal directions of this tensor are assumed to be coaxial with those of the permeability tensor. One of the main reasons for the widespread use of Oda's model is the balance between simplicity and accuracy. The approach is based on a fast algorithm that does not require explicit flow modeling. This makes it particularly suitable for integration into commercial software used for permeability estimation in fractured rock formations. Despite its strengths, Oda's approach has a number of limitations. Perhaps the most restrictive one is the implicit assumption that all fractures in the network are interconnected. Ignoring the presence of discontinuous or dead-end fractures results in an overestimation of directional permeability [46-48]. A further limitation is the sensitivity of the model to fracture aperture values, which themselves are extremely uncertain. The fracture aperture is influenced by a multitude of variables, most notably changes in stress state within the rock mass, making measurement problematic. Uncertainty in aperture estimation represents a tremendous hurdle for applying Oda's model to real-world engineering problems [49].

Another practical technique for estimating permeability in fractured rock masses is the pipe network model. This model considers the fracture domain as a network of interconnected pipes/channels, with each one characterized by the fracture aperture and connectivity (cf. refs. [50-51]). In this method, the fractured rock is considered a discrete lattice system, and flow is along specified flow paths. By reducing the complicated geometry of fractures to a structured network, the pipe network model allows computationally efficient simulation of fluid flow in fractured media that still retains important hydraulic features. The pipe network model typically uses graph theory algorithms to sort fractures based on their intersection with other fractures. The main purpose of this sorting is to be able to remove isolated or dead-end fractures with little to no contribution to overall fluid flow. By doing this, the model ensures that only hydraulically active paths are preserved. While this is a useful simplification of complex fracture networks, it does come with certain limitations. Among its major weaknesses is the fact that, in its original formulation, the model assumes the intact rock matrix to be perfectly impervious. This means that it ignores any flow of fluid through the rock itself, which for certain types of rocks is quite restrictive [52]. Some of the more recently introduced modifications account for fluid transmissivity across the porous matrix. In these updated approaches, the intact rock domain is discretized with structured or unstructured elements, which are then embedded within the existing pipe network framework (cf. ref. [53]). However, it is still unclear if such "matrix pipe" approximations are sufficiently accurate.

A more realistic and detailed description of the flow process can be achieved by invoking other modeling approaches that include the implementation of a constitutive law with embedded discontinuity [54]. In the latter approach, hydraulic conductivity in the vicinity of fractures is evaluated by a volume-averaging technique applied to the fluid pressure gradient. The method captures the localized effect of fractures on permeability by utilizing the formulation, which eliminates the need for explicit discretization of individual discontinuities. Furthermore, unlike other approaches that require additional degrees of freedom or specialized numerical techniques, this methodology operates within the standard finite element framework, and it easily integrates into the existing commercial finite element software. This makes it a very useful and practical tool for simulating flow through fractured rock masses.

1.2 Scope of the Work

This thesis consists of four chapters, each of them covering a particular aspect of the research. Chapter 2 provides the formulation of constitutive relations governing the mechanical response of Cobourg limestone. A new approach is developed for describing the inherent anisotropy of this material. In the proposed approach, the heterogeneity of fabric is quantified by employing the mean intercept length (MIL) as the primary descriptor. This descriptor is then correlated with strength anisotropy through the concept of a fabric tensor. A new mathematical representation is established, which requires the specification of the preferred material direction and does not explicitly employ the eigenvalues of the fabric tensor. The latter were previously considered as best-fit approximation coefficients in the expression for the anisotropy parameter. The chapter also includes a numerical study related to the simulation of triaxial tests conducted on differently oriented samples of Cobourg limestone.

Chapter 3 examines different methodologies used to estimate the equivalent hydraulic conductivity tensor in fractured rock masses. Simplified approaches, such as Oda's notion of permeability tensor and the pipe network model, are employed first. The results are then compared with those generated by a finite element analysis incorporating a constitutive law with embedded discontinuity (CLED), which has so far been used mainly for mechanical analysis. A number of numerical examples involving fluid flow in the presence of discrete fracture networks are given, and the principal values/directions of the equivalent conductivity tensor are compared. The limitations of simplified methodologies are pointed out and a pragmatic hybrid approach is suggested, which employs the estimates of eigenvectors based on pipe network model, combined with CLED simulations for flow along the principal directions. Finally, Chapter 4 summarizes the findings and provides recommendations for future research.

CHAPTER 2

On the mechanical anisotropy of argillaceous Cobourg limestone: fabric tensor approach[1]

Interpretation of the mechanical behavior of Cobourg limestone requires information on its heterogeneous fabric and how it influences the strength and deformation characteristics. The anisotropic nature of this rock is largely the result of the presence of argillaceous inclusions, whose volume fraction differs from sample to sample. The objective of this chapter is the quantification of fabric anisotropy based on stereological concepts, with the mean intercept length (MIL) as the primary descriptor. The correlation between fabric characteristics and the strength anisotropy is obtained by invoking the concept of fabric tensor. Experimental data, including the results of triaxial tests, are analyzed to assess the influence of the distribution of argillaceous partings on the mechanical response. The outcome constitutes the basis for defining an anisotropic failure criterion as well as developing a constitutive framework that takes into account both fabric orientation and heterogeneity.

2.1 Specification of strength anisotropy parameter for Cobourg limestone

The internal structure of Cobourg limestone can be described using stereological principles that provide a mathematical framework for interpreting three-dimensional (3D)

[1] Note: This chapter includes substantial parts of the article published in the International Journal of Rock Mechanics and Mining Sciences:
S. Pietruszczak and P. Pakdel, On the mechanical anisotropy of argillaceous Cobourg limestone: Fabric tensor approach, *Int. J. Rock Mech. Min. Sci*., vol. 150, p. 104953, 2022. https://doi.org/10.1016/j.ijrmms.2021.104953

microstructural features from observations on two-dimensional (2D) planar sections. Since direct 3D observation of complex geological materials is often impractical, stereology offers an efficient approach to the analysis of rock fabric using quantitative descriptors.

Stereological methods rely on the use of unbiased test probes, which ensure that the measurements represent the inherent characteristics of the rock without any observational bias. Among a number of stereological techniques, lineal probes play an important role in quantifying the direction-dependent fabric characteristics. These probes are evenly distributed across the sample and can be rotated from a reference orientation into other sampling directions. This variation aids in extracting orientation-sensitive microstructural information that is critical for analyzing material anisotropy in Cobourg limestone.

For any specific fabric descriptor, its spatial distribution may be assumed in the form suggested by Kanatani (cf. ref. [55]). The latter employs a scalar-valued function defined as

$$f(\nu_i) = C\left(1 + D_{ij}\nu_i\nu_j + D_{ijkl}\nu_i\nu_j\nu_k\nu_l + \cdots\right) \tag{2.1}$$

Here, C represents the orientation average of the fabric descriptor, and D's are symmetric, traceless, even-ranked tensors that characterize the distribution bias, i.e. deviation from an idealized isotropic structure. The simplest approximation is apparently the one that includes only the second-order tensor, i.e.

$$f(\nu_i) = C\left(1 + D_{ij}\nu_i\nu_j\right); D_{ii} = 0; D_{ij} = D_{ji}; \nu_i\nu_i = 1 \tag{2.2}$$

An alternative form of eq. 2.2 can be written as

$$f(\nu_i) = 3CF_{ij}\nu_i\nu_j; F_{ij} = \frac{1}{3}\left(\delta_{ij} + D_{ij}\right); F_{ii} = 1 \tag{2.3}$$

where F_{ij} is a normalized fabric tensor, which provides a dimensionless representation of fabric anisotropy. Assuming that the principal material axes (x_1, x_2, x_3) are defined in terms of base vectors (t_i, n_i, s_i), respectively, the spectral decomposition of this tensor may be expressed in the form

$$F_{ij} = (\lambda_1 - \lambda_3)t_i t_j + (\lambda_2 - \lambda_3)n_i n_j + \lambda_3\delta_{ij} \tag{2.4}$$

where λ's are the eigenvalues which define the principal directions of anisotropy.

As demonstrated in the follow-up section, the fabric of Cobourg limestone may be considered as transversely isotropic, implying that it has a preferred orientation along which the in-plane properties remain isotropic. Assuming that n_i represents this preferred direction, there is $\lambda_1 = \lambda_3$, which in view of $F_{ii} = 1$ gives

$$F_{ij} = \lambda_1\delta_{ij} + (1 - 3\lambda_1)n_i n_j \tag{2.5}$$

Thus, the deviatoric operator in eq. 2.3 can be defined as

$$D_{ij} = 3F_{ij} - \delta_{ij} = 3\left[\lambda_1\delta_{ij} + (1 - 3\lambda_1)n_i n_j\right] - \delta_{ij} \tag{2.6}$$

which can be further simplified to

$$D_{ij} = 3(1 - 3\lambda_1)\Omega_{ij}; \quad \Omega_{ij} = n_i n_j - \delta_{ij}/3 \tag{2.7}$$

To establish a direct connection between the strength properties of the Cobourg limestone and its fabric structure, an anisotropy parameter η, as suggested in ref. 56, is now introduced. This parameter is designed to quantify the influence of fabric orientation on the material's strength characteristics. It is defined as a projection of D_{ij} onto the loading direction l_i, viz.

$$\eta = a_1 + a_2 D_{ij} l_i l_j \tag{2.8}$$

where the coefficients a's are material constants. The loading direction is defined as follows:

$$l_i = \frac{L_i}{(L_k L_k)^{1/2}}; L_i = L_j e_i^{(j)}; L_j = (\sigma_{j1}^2 + \sigma_{j2}^2 + \sigma_{j3}^2)^{1/2} \tag{2.9}$$

In this representation, the components of L_i describe the magnitudes of traction vectors acting on planes normal to the principal material axes $e_i^{(1)} = t_i, e_i^{(2)} = n_i, e_i^{(3)} = s_i$. By substituting equation 2.7 into equation 2.8 and rearranging the terms, we obtain

$$\eta = \hat{\eta}[1 - A(1 - 3\zeta^2)]; \quad \zeta = n_i l_i \tag{2.10}$$

where $A = a_2(1 - 3\lambda_1)/a_1 = const.$ and $\hat{\eta} = a_1$ represents the orientation average of η. Note that if the preferred material direction n_i is known a priori, the constants governing the strength variation A and $\hat{\eta}$ can be directly estimated from experimental data defining the spatial variation of strength. Consequently, no explicit information on eigenvalue (λ_1) of the fabric tensor is needed, which implies that no explicit fabric measure needs to be employed in the formulation. In general, however, a fabric descriptor is necessary when dealing with a complex heterogeneous fabric in order to estimate the preferred material orientation n_i.

The interpretation the experimental data for Cobourg limestone presents some challenges. While there is clear evidence that the rock's strength is influenced by sample orientation, the results exhibit significant scatter across all tested orientations. This variability most likely results from the heterogeneous nature of the fabric, where the distribution and composition of mineral inclusions vary at a microstructural level.

Unfortunately, previous experimental studies on Cobourg limestone have not directly correlated mechanical behavior with fabric characteristics, leaving a gap in understanding the exact role of material anisotropy. In this study, we propose that the strength and deformation properties are affected not only by the sample orientation but also by the volume fraction of argillaceous inclusions μ. This suggests that anisotropy in mechanical properties is not solely dependent on directional alignment but also on the inherent variability in the composition of the rock.

To account for this, the notion of anisotropy parameter, eq. 2.10, is enhanced by incorporating the variability in the orientation average $\hat{\eta}$ as well as the bias parameter A, which are both assumed to be a function of the volume fraction μ. Thus,

$$\eta = \eta(l_i, \mu) = \hat{\eta}[1 - A(1 - 3\zeta^2)]; \quad \hat{\eta} = \hat{\eta}(\mu), \qquad A = A(\mu) \tag{2.11}$$

Further discussion on this general form is provided in Section 2-3.

2.2 Description of fabric of Cobourg limestone

2.2.1 Introduction

The quantitative fabric measure employed in this work is the Mean Intercept Length (MIL). The concept of MIL is fundamentally rooted in stereology, and its definition involves counting the length of intercepts along a set of parallel test lines passed through the sample at different discrete orientations. Thus, for each specific test line, the MIL measures the distance travelled in a reference material before intersecting another phase or component. This measure has been employed here to quantify the fabric of the Cobourg limestone.

The MIL can be determined from binary images or volume data. The procedures are computationally intensive, so that various techniques have been developed to increase their efficiency. The classical procedure of computing MIL is a Monte Carlo or a grid sampling procedure, which involves passing a large number of test lines through the microstructure in several orientations. In the early developments, the analysis was restricted to two-dimensional sections and performed by means of overlaying a grid of parallel lines with known spacing and length at a certain angle [57]. This would be repeated at multiple angles. Nowadays, with digital images, this process is automated and can be used for complex 3D structures.

The following section describes the mathematical formulation of the MIL descriptor as well as the notion of a fabric tensor. It also describes the methodologies for estimating MIL through image analysis and their use in quantifying the fabric anisotropy.

2.2.2 Mathematical definition of MIL and its identification for Cobourg limestone

In order to formally define the MIL, consider an array of evenly spaced parallel test lines. Denote as $L(\nu_i)$ the total length of these lines in a given direction ν_i . Furthermore, let $\Sigma I(\nu_i)$ represents the length of all intersections of these test lines with the darker argillaceous inclusions, and let $N(\nu_i)$ be the total number of intercepts.

Note that all the linear measurements are typically made inside a reference volume, which is thought to be a sphere with radius R. To ensure uniformity with respect to the orientation of measurements, the centroid of this reference volume is chosen as the origin for the Cartesian coordinate system.

The mean intercept length (MIL) is a scalar-valued function of ν_i, and is defined as

$$MIL(\nu_i) = \mu \frac{L(\nu_i)}{N(\nu_i)} = \frac{\Sigma I(\nu_i)}{L(\nu_i)} \frac{L(\nu_i)}{N(\nu_i)} = \frac{\Sigma I(\nu_i)}{N(\nu_i)} \tag{2.12}$$

where μ represents the lineal fraction of the darker argillaceous phase along a specific direction ν_i. It is important to note that μ is an orientation independent quantity, meaning that any influence of material anisotropy is captured by the second term. As mentioned earlier, the information on the volume fraction is of importance, as its value affects the mechanical properties of Cobourg limestone.

The general mathematical form used to describe the fabric measure of Cobourg limestone is taken as (cf. ref. [56])

$$MIL(\nu_i) = C\left(1 + D_{ij}\nu_i\nu_j + \sum_{k=2}^{l} a_{k-2}\left(D_{ij}\nu_i\nu_j\right)^k\right) \qquad 2.13$$

This representation incorporates a symmetric, traceless tensor D_{ij}, appearing in eq. 2-1, which characterizes deviations from an idealized isotropic structure while C is a constant. For a smooth orthogonal anisotropy, the mathematical representation can be simplified by retaining only the first-order term in D_{ij}, thus reducing it to the form analogous to that of eq. 2.2, i.e.

$$MIL(\nu_i) \approx C\left(1 + D_{ij}\nu_i\nu_j\right) \qquad 2.14$$

In this case, the coefficient C defines the mean value of the MIL descriptor. The components of D_{ij}, as well as the value of C, can be identified from the best-fit approximation to the measurements associated with each discrete orientation ν_i. An important step in this approach is identifying the principal directions of fabric anisotropy. Given the individual components of the operator D_{ij}, these directions can be obtained by solving the eigenvalue problem, viz.

$$\left(D_{ij} - \lambda\delta_{ij}\right)e_j^{(\alpha)} = 0; \quad D_{ij} = \lambda_1 t_i t_j + \lambda_2 n_i n_j + \lambda_3 s_i s_j \qquad 2.15$$

where $e_i^{(\alpha)}(\alpha = 1,2,3)$ are again the base vectors which define the orientation of material axes (i.e., $e_i^{(1)} = t_i, e_i^{(2)} = n_i, e_i^{(3)} = s_i$) and λ's are the respective eigenvalues of D_{ij}.

Note that an alternative way to define the MIL descriptor is to employ eq. 2.3, in which case

$$MIL(\nu_i) \approx 3CF_{ij}\nu_i\nu_j; \quad F_{ij} = \frac{1}{3}\left(\delta_{ij} + D_{ij}\right); F_{ii} = 1 \qquad 2.16$$

where F_{ij} is the normalized fabric tensor.

The theoretical formulation outlined above, viz. eqs. 2.12 and 2.16, has been applied to the quantification of fabric for a sample of Cobourg limestone using the raw microstructural data collected at McGill University (cf. ref. 58). In that study, a cuboidal specimen was divided into several thin slabs, and the spatial distribution of mineral inclusions was then mapped out. The surface contours of the lighter and darker regions of each slab were identified using photographic images of each surface area combined with digital imaging techniques. By using Matlab's image processing software, the photos were then converted into binary black and white images.

The sample analyzed in this study was a cylindrical rock core with a diameter of 150 mm and a length of 310 mm. The specimen was divided into 13 separate discs, and each slice was examined to quantify the spatial variation in mineral distribution. An example of a photographed and digitized image for one of those disks is shown in Fig. 2-1.

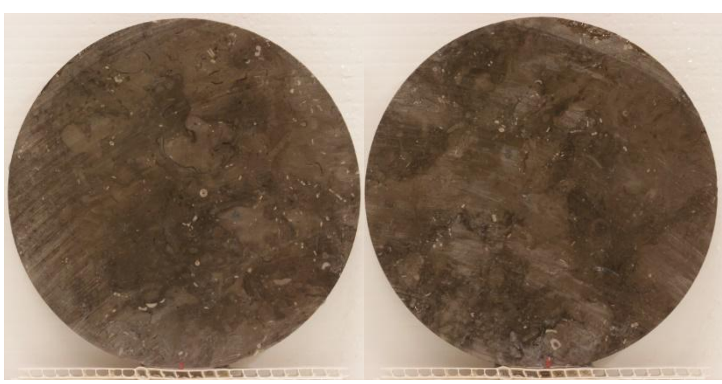

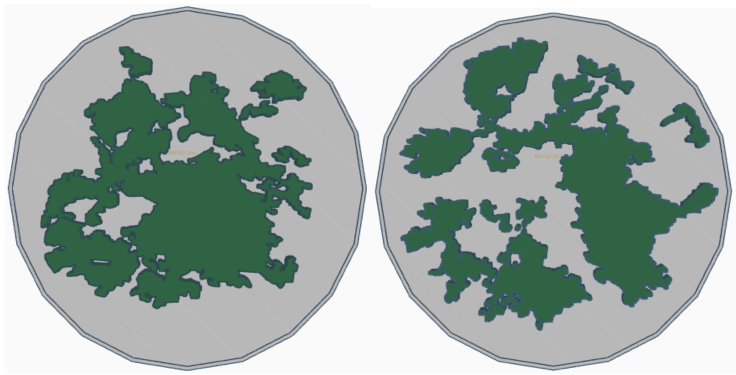

Fig. 2-1. Photographic and digitized images of top (right) and bottom (left) surfaces of disk #5

For the analyzed specimen, the function $MIL(\nu_i)$ defining the distribution of the mean size of the gray facies has been determined by using BoneJ, an open-source research code (ref. 59). The code works as a plugin within ImageJ, a widely used Java-based image processing software. The BoneJ package was developed for applications in biomechanics to quantify the trabecular bone architecture as well as the whole bone shape analysis. The MIL algorithm within BoneJ employs either a single sphere positioned at the image centroid or multiple randomly placed spheres to ensure high precision in the case of a complex fabric.

The BoneJ plugin's anisotropy function executes the following steps: (1) generate n random directions uniformly distributed on the unit sphere, (2) for each direction, trace parallel lines through the image stack and record all the points where the line passes from background to the foreground (i.e., encounters a phase boundary), (3) compute the mean intercept length for the specified orientation forming a MIL vector of that length in the given direction, (4) collect all these MIL vectors (each can be envisioned as a point from the origin in 3D space) and fit an ellipsoid to them, and finally (5) extract the fabric tensor and degree of anisotropy from the ellipsoid's axes.

This algorithm is stochastic (because of random sampling), so it often runs multiple times to ensure a stable result. The accuracy improves with an increasing number of sample lines and directions. Typically, hundreds or even thousands of line samples are used, which is feasible with modern computing. The results are given in terms of the three principal values and the corresponding eigenvector directions.

It is noted that in BoneJ code, the degree of anisotropy is mathematically defined using a second-rank tensor originally introduced by Harrigan & Mann (ref. 60). Thus, the results obtained from BoneJ were then reinterpreted within the context of eq. 2.14 and expressed in terms of the traceless tensor D_{ij} to provide quantification of fabric anisotropy consistent with definition 2-12.

The core findings from this analysis are presented in Figs. 2-2 and 2-3. The analyzed sample is cylindrical, with a diameter of 150 mm and a length of 310 mm. The computed values of the fabric tensor F_{ij}, aligned with the original coordinate system (x, y, z) attached to the sample, and the orientation average of MIL are estimated as

$$F_{ij} = \begin{pmatrix} 0.38418 & -0.00516 & -0.00002 \\ -0.00516 & 0.23166 & -0.00105 \\ -0.00002 & -0.0010 & 0.38416 \end{pmatrix}; C = 13.71mm$$

In this case, the principal material axes are defined by the base vectors

$$t_i = (-0.994, 0.034, -0.108); n_i = (0.034, 0.999, 0.007); s_i = (0.108, 0.003, -0.994)$$

while the eigenvalues of F_{ij} are $F_1 = 0.38, F_2 = 0.23, F_3 = 0.38$.

Fig. 2-2 shows the distribution of $MIL(v_i)$ within the conjugate planes of the principal material system, based on the mathematical representation in eq. 2.14. The MIL measurements along the principal axes (x_1, x_2, x_3) are 15.81 mm, 9.53 mm and 15.81 mm, respectively.

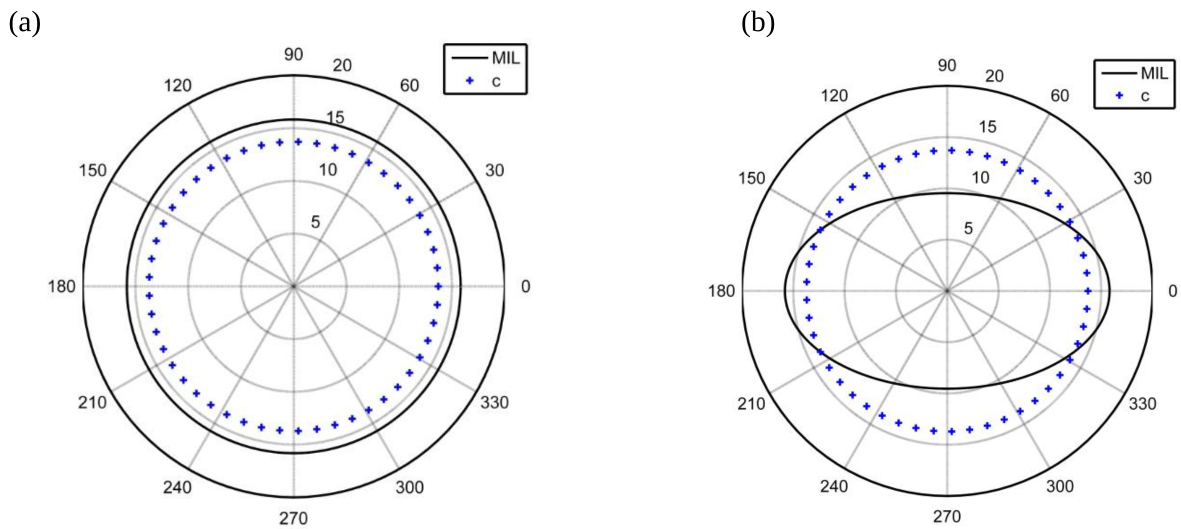

Fig. 2-2. 2D plots of best fit approximation of MIL in principal plane view- polar coordinates a) x_1–x_3 plane b) x_1–x_2 and x_3–x_2 plane

For the geometric visualization of the fabric tensor, the method described by Westin et al. (ref. 61) was used. This technique maps any second-order symmetric tensor, say A_{ij}, to a three-dimensional object having three components: (i) a line segment directed towards the principal direction of the fabric tensor, with its length proportional to the largest eigenvalue, (ii) a disk displaying the spread of the plane that is defined by the two largest eigenvectors, capturing the directional preference in the rock structure, and (iii) a sphere with the radius proportional to the smallest eigenvalue.

The mathematical relation used for this geometric representation takes the form

$$A_{ij} = (\lambda_1 - \lambda_2)A_{ij}^l + (\lambda_2 - \lambda_3)A_{ij}^p + \lambda_3 A_{ij}^s \qquad 2.17$$

where

$$A_{ij}^l = e_i^{(1)}e_j^{(1)}; \quad A_{ij}^p = e_i^{(1)}e_j^{(1)} + e_i^{(2)}e_j^{(2)}$$
$$A_{ij}^s = e_i^{(1)}e_j^{(1)} + e_i^{(2)}e_j^{(2)} + e_i^{(3)}e_j^{(3)} \qquad 2.18$$

Fig. 2-3 shows the geometric visualization of the normalized fabric tensor F_{ij}, where the line segment has a unit length (1), the disk radius is given by (λ_1/λ_3), and the sphere radius is (λ_2/λ_3).

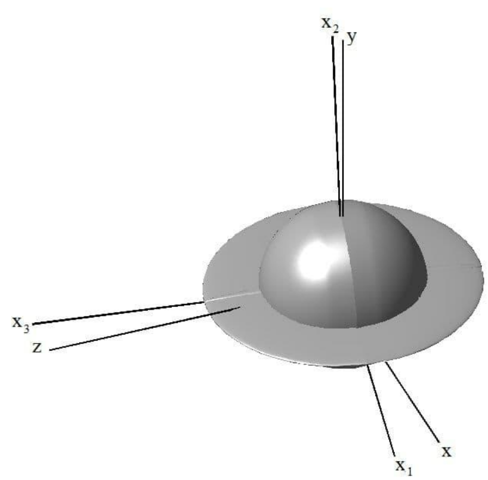

Fig. 2-3. Geometric representation of the normalized fabric tensor

The analysis provided above shows that the principal directions of fabric are virtually colinear with the orientation of the sample. It was indicated in ref. 8 that larger blocks of limestone were selected based on the visibility of the stratification, and the blocks were quarried parallel to or normal to the stratification plane. The sample analyzed in this study was cored perpendicular to the argillaceous partings; hence, these findings support the argument that anisotropy in the material is primarily due to the sedimentation process and the elongated argillaceous regions are in the stratification planes.

In terms of the type of inherent anisotropy, it is evident that $\lambda_1 \approx \lambda_3$, so that a transversely isotropic approximation is adequate for describing both mechanical and hydraulic properties. As mentioned before, material heterogeneity associated with variations in the volume fraction of argillaceous inclusions (μ) is another key factor that will influence the material's response.

In general, the orientation of fabric will not be uniform throughout the rock mass. Also, in the case of samples extracted from the same location, the mechanical properties are likely to be affected by the size of the specimen, which is due to variability in the mineral composition and distribution. In this case, the orientation of the material axes will remain the same; however, the volume fraction μ of the argillaceous partings that affects the strength and deformability properties could be different, which might impact the mechanical response. In order to address this issue, a microstructural assessment was conducted for the lower half of the cylindrical specimen. This section, encompassing half of the original sample (i.e., the diameter of 150 mm and the length of 155 mm), was also subjected to the same stereological analyses as that applied to the whole sample. In this case, the components of the fabric tensor and the orientation-average of the mean intercept length (MIL) were estimated as

$$F_{ij} = \begin{bmatrix} 0.3944 & -0.0046 & 0.0003 \\ -0.0046 & 0.2120 & -0.0130 \\ 0.0003 & -0.0130 & 0.3936 \end{bmatrix}; \;\; C = 13.36$$

while the principal material axes were defined by the base vectors

$$t_i = (0.998, 0.028, -0.047);\ n_i = (-0.0250, -0.997, -0.0710)\ \ s_i = (0.049, -0.070, 0.996)$$

It can be seen while the preferred material direction has not changed, the volume fraction μ of the argillaceous inclusions exhibited a notable difference when compared to the entire sample, i.e.

whole sample: $\mu = 0.35$; bottom half: $\mu = 0.30$

Summarizing the above findings, it can be concluded that the strength properties of Cobourg limestone can be characterized by transverse isotropy and the preferred material direction n_i is along the normal to the stratification planes. This conclusion stems from the use of the mean intercept length (MIL) as the fabric descriptor. However, as pointed out in ref. 23, other conjugate descriptors that employ stereological measurements tend to predict similar directions of material axes. Thus, this assertion appears to be more widely supported. Furthermore, the mechanical properties of Cobourg limestone depend not only on the fabric orientation but also on the variability in the volume fraction μ of the argillaceous facies. Consequently, the latter needs also to be incorporated in the general formulation of the problem.

2.3 Formulation of constitutive law incorporating a fabric descriptor

2.3.1 Specification of conditions at failure

Despite extensive numerical investigation, a direct correlation between the mechanical response of Cobourg limestone and its fabric has not been explicitly established. This limitation makes it difficult to draw quantitative conclusions in relation to anisotropy in mechanical properties. The latter is evident from Fig. 2-4, presented earlier in Chapter 1, where the distribution of uniaxial compressive strength is plotted (after ref. [14]). The scatter in the experimental data, even for samples with the same nominal orientation, is very significant. This can likely be attributed to heterogeneities in the fabric, specifically the variability in the volume fraction of argillaceous parting.

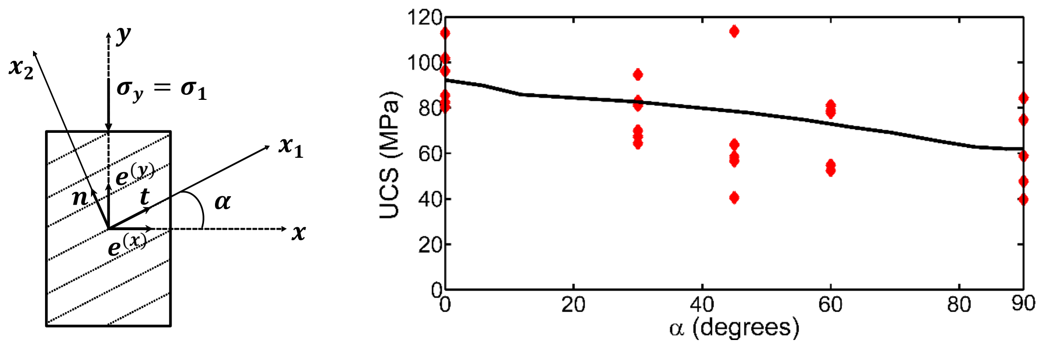

Fig. 2-4. Uniaxial compressive strength (UCS) for different orientations of specimens (after ref. [14])

The experimental data used in the current study is largely based on the results obtained at McGill University (ref. 10). The tests reported in this reference were conducted only on specimens which were either parallel or perpendicular to the stratification planes. The testing program was quite comprehensive and involved, among others, a series of Obert-Hoek triaxial cell tests carried out at confining pressures ranging from 5MPa to 60MPa.

These tests indicated that the conditions at failure can be approximated by a linear envelope, which is characteristic of the Mohr-Coulomb criterion. However, the standard representation needs to be enhanced to incorporate the dependence of strength on the sample orientation as well as the volume fraction μ . To address this, the failure function can be defined in the form similar to that employed in ref. [62], i.e.

$$F = \sqrt{3}\bar{\sigma} - \eta g(\theta)(\sigma_m + \bar{c}); \quad \eta = \eta(l_i, \mu) \tag{2.19}$$

where

$$\bar{\sigma} = (J_2)^{\frac{1}{2}}; \quad \sigma_m = -\frac{1}{3}I_1; \quad \theta = \frac{1}{3}sin^{-1}\left(\frac{-3\sqrt{3}}{2}\frac{J_3}{\bar{\sigma}^3}\right);$$

$$g(\theta) = \frac{3 - sin\,\phi}{2\sqrt{3}\,cos\,\theta - 2\,sin\,\theta\,sin\,\phi}; \ \ \eta = \frac{6\,sin\,\phi}{3 - sin\,\phi}; \quad \bar{c} = c\,cot\,\phi \tag{2.20}$$

In the above equations, I_1, J_2, J_3 are the basic invariants of stress tensor/deviator, $\theta$is the Lode's angle, while ϕ and c represent the angle of friction and cohesion, respectively. Moreover, $\bar{c}$ is the strength under hydrostatic tension, which is orientation-independent, while $\eta = \eta(l_i, \mu)$ is the strength anisotropy parameter defined by representation 2.11. The specification of this function requires a correlation between the orientation-dependent strength anisotropy and the volume fraction of argillaceous partings.

As stated before, there is no explicit information on the volume fraction μ of the gray argillaceous facies within the tested specimens. At the same time, however, the experimental data reported in ref. 8 includes photographic images of the four sides of each triaxial specimen. Those photographs were thus converted into binary black and white images using processing software available in the MATLAB package. Subsequently, the BoneJ open-source plugin module was used to calculate the areal fraction of the dark facies, representing the clayey inclusions, for each of the four images. The mean of these fractions was considered to be a measure of the overall volume fraction of the argillaceous material. An example of such an image-based assessment is provided in Fig. 2-5. The figure includes the binary images of the triaxial specimen with horizontal stratification planes for which the estimated argillaceous fraction is 0.311.

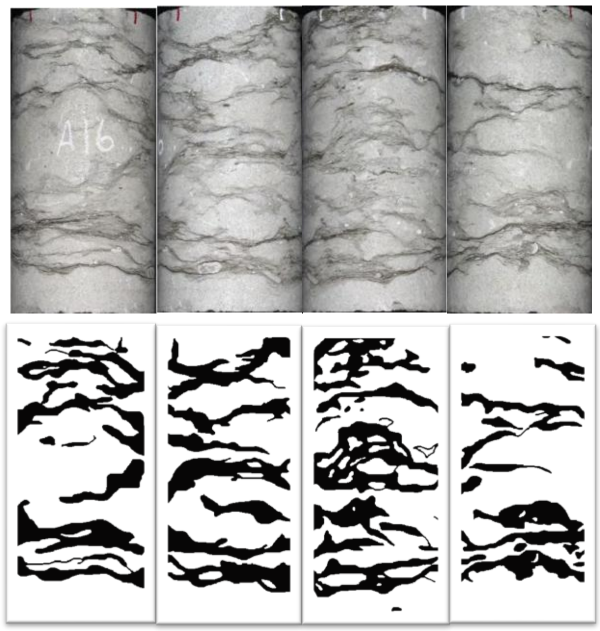

Fig. 2-5. Binary surface images of four sides of a triaxial specimen (sample HA16, ref. [10]); μ =0.311

To establish a statistically representative approximation, the identification of the material anisotropy function $\eta = \eta(l_i, \mu)$ incorporated a set of results from 19 triaxial tests (cf. Table 2-1). As mentioned before, all tests involved a specimen with argillaceous partings oriented either horizontally or vertically. For each test, given the stress state at failure, the value of the strength parameter η and the corresponding loading direction l_i was determined. To facilitate the analysis, the coordinate system was aligned with the principal material axes, as depicted in Fig. 2-4. In this case $\zeta = n_i l_i = l_2$, so that eq. 2.11 simplifies to

$$\eta = \hat{\eta}[1 - A(1 - 3l_2^2)]; \hat{\eta} = \hat{\eta}(\mu), A = A(\mu) \qquad 2.21$$

where for triaxial loading conditions

$$l_2^2 = \frac{p_0^2 \, sin^2 \, \alpha + \sigma_y^2 \, cos^2 \, \alpha}{2p_0^2 + \sigma_y^2}; p_0 = \left(\sigma_y + 2\sigma_x\right)/3, cos \, \alpha = n_i e_i^{(y)} \qquad 2.22$$

Based on the experimental data reported in ref 10, the parameter $\bar{c}$ was estimated as 43 MPa. It is noted that this parameter does not have any direct physical significance as for failure in the tension regime the Rankine cut-off criterion is used. The latter stipulates that, for any orientation of the sample, the tensile strength is below $\bar{c}$. Thus, the primary role of $\bar{c}$ is to facilitate the determination of η, the value of which, for a given stress state, has been obtained directly from eq. 2.19.

Table 2-1. Characterization of selected triaxial samples(*)

Sample #	Volume fraction μ	σ_3 (MPa)	η	l_2^2
1 (H)	0.277	10	1.458	0.990
2 (H)	0.241	10	1.422	0.989
3 (H)	0.270	10	1.515	0.991
4 (V)	0.190	10	1.606	0.004
5 (V)	0.195	10	1.609	0.004
6 (V)	0.189	10	1.540	0.004
7 (V)	0.185	10	1.535	0.004
8 (H)	0.311	40	1.466	0.958
9 (H)	0.258	40	1.479	0.959
10 (H)	0.326	40	1.508	0.962
11 (V)	0.218	40	1.548	0.017

12 (V)	0.188	40	1.553	0.017
13 (V)	0.277	40	1.546	0.018
14 (H)	0.232	60	1.442	0.941
15 (H)	0.262	60	1.66	0.944
16 (H)	0.299	60	1.417	0.938
17 (V)	0.169	60	1.501	0.026
18 (V)	0.192	60	1.461	0.028
19 (V)	0.185	60	1.452	0.029

(*) Orientation of argillaceous partings: nominally horizontal (H) and vertical (V)

The dataset provided in Table 2-1, which correlates the strength parameter with both the loading direction and the volume fraction, has now been used to identify the function $\eta = \eta(l_i, \mu)$. In this process, a linear dependence of parameters $\hat{\eta}$ and A on the value of μ, has been assumed, i.e.

$$\hat{\eta} = a_1 + a_2\mu; A = b_1 + b_2\mu \tag{2.23}$$

Incorporating this relation into eq. 2-21, the resulting expression becomes

$$\eta = (a_1 + a_2\mu)[1 - (b_1 + b_2\mu)(1 - 3l_2^2)] \tag{2.24}$$

or, in an equivalent form

$$\eta = (a_1 - a_1b_1) + [a_2 - (a_1b_2 + a_2b_1)]\mu - (a_2b_2)\mu^2 + (3a_1b_1)l_2^2 + 3(a_1b_2 + a_2b_1)\mu l_2^2 + (3a_2b_2)\mu^2 l_2^2 \tag{2.25}$$

Fig. 2-6 shows the best-fit approximation, based on the representation 2.24, in the affine space (μ, η, l_2^2). The corresponding approximation coefficients are:

$$a_1 = 0.6203, a_2 = 1{,}379, b_1 = -0.0573, b_2 = -0.0137$$

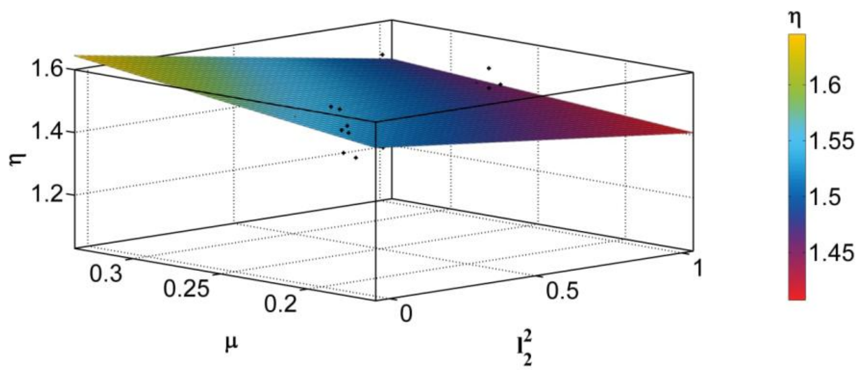

Fig. 2-6. The variation of strength parameter with volume fraction of argillaceous facies and the loading direction

The values specified above fully define the failure criterion 2.19 in which the strength anisotropy parameter is given by eq. 2.21, while the orientation-average $\hat{\eta}$ and the bias parameter A are described by eq. 2.22.

In order to assess the predictive abilities of the proposed criterion, its functional form has been used to estimate the axial strength σ_f for a number of specimens tested under triaxial conditions. These tests included some of the tests listed in Table 2-1 as well as other experiments performed at confining pressures of 20 MPa and 50 MPa, which were not explicitly used for the identification of approximation coefficients. The information on the latter tests is given in Table 2-2. Fig. 2-7 shows a bar graph comparing the experimental data with the numerical predictions of axial strength. It is evident that the quantitative results are fairly consistent with the reported data. This indicates that the proposed anisotropic failure criterion is indeed able to adequately describe the strength characteristics of Cobourg limestone despite the simplifications that stem from limited information on the material fabric.

Table 2-2. Additional tests used for simulations

Sample #	μ	σ_3 (MPa)	$\sigma_1 = \sigma_f$ (MPa)
20 (H)	0.275	20	207.29
21 (V)	0.256	20	229.31
22 (H)	0.374	50	325.80
23 (V)	0.173	50	328.11

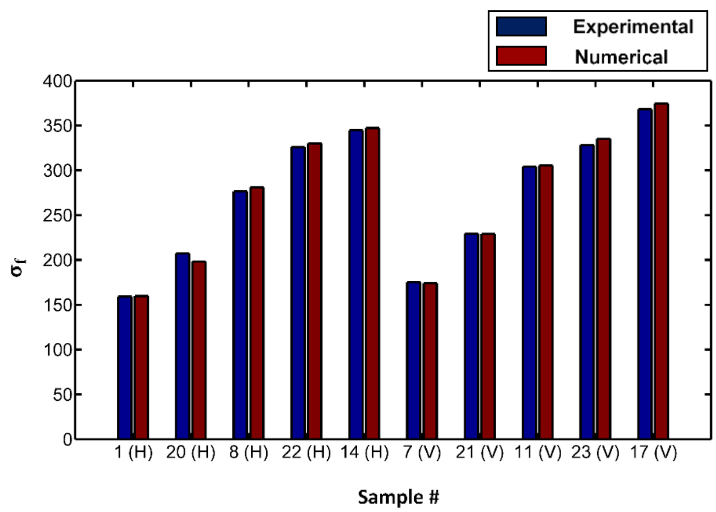

Fig. 2-7. The predicted strength of triaxial specimens with different volume fractions of argillaceous partings

2.3.2 Specification of deformation characteristics

In the case of an elastoplastic material, the mechanical response may be defined by adopting the functional form of the yield surface, which is similar to representation 2.19, i.e.

$$f = \sqrt{3}\bar{\sigma} - \vartheta g(\theta)(\sigma_m + C) = 0; \vartheta = \eta(l_i, \mu)\frac{\xi\kappa}{B + \kappa}; d\kappa = \left(\frac{2}{3} de_{ij}^p de_{ij}^p\right)^{1/2} \qquad 2.26$$

where e_{ij}^p is the deviatoric part of the plastic strain, and B and ξ are material parameters. According to the hardening rule, for $\kappa \to \infty$ there is $\vartheta \to \xi\eta$, where $\xi > 1$. The parameter ξ is introduced to represent the transition to localized deformation, which is assumed to occur at $\vartheta = \eta$ (cf. ref. [63]). The latter equality implies that $f = F$, so that the conditions at failure are consistent with the Mohr-Coulomb criterion (eq. 2.19). Note that, in general, the onset of localized deformation may be considered as a bifurcation problem [64].

To accurately represent the transition from compaction to dilatancy that is commonly observed in sedimentary rocks, a non-associated flow rule is employed with the plastic potential defined as

$$\psi = \sqrt{3}\bar{\sigma} + \eta_c g(\theta)(\sigma_m + C)\, ln\frac{(\sigma_m + \bar{c})}{\sigma_m^0} = 0 \qquad 2.27$$

where η_c is a dilatancy coefficient defined as $\eta_c = \upsilon\eta$, with υ considered as a material constant. Given the definition of the yield and plastic potential surface, eqs. 2.26 and 2.27, the constitutive relation can be derived following the standard plasticity procedure. This involves employing the additivity of elastic and plastic strain rates together with the consistency condition $df = 0$. The details in this respect are provided, for example, in ref. [62].

In order to illustrate the performance of the proposed deviatoric hardening framework, numerical simulations of the deformation process for compression tests listed in Tables 1-2 have been provided. The analysis requires the specification of elastic moduli as well as parameters governing the plastic deformation, i.e. B, η_c. The experimental data in ref. [10] indicates that the elastic properties of the material are not significantly influenced by changes in confining pressure and/or the volume fraction of argillaceous partings. Their values have been taken as

$$\mathrm{E_h} = 21\mathrm{GPa}, \mathrm{E_v} = 25\mathrm{GPa}, \nu_{\mathrm{hh}} = \nu_{\mathrm{vh}}{=}0.25, \mathrm{G_{vh}} = 9\mathrm{GPa}$$

In the elastoplastic regime, the condition for a transition from compaction to dilation was defined, based on experimental data, as $\eta_c = 0.9\eta$. Furthermore, the value of ξ was set to 1.2, and B was calibrated through a trial-and-error process to best fit the deviatoric characteristics of two randomly selected tests. The estimated value of B was 0.0003, which is relatively low, suggesting that before localization the material stiffness is nearly linear and, again - not significantly affected by the volume fraction of argillaceous facies.

The results of numerical simulations are shown in Fig. 2-8. The analysis involves both vertical and horizontal samples tested within the range of confinements of 10-60 MPa. The transition to localized deformation, which is set to occur at $\vartheta = \eta$, is indicated here by an arrow. No volume change characteristics are included here, as these were not reported in the experiments. Again, the results of simulations seem to be fairly consistent with the test data. This indicates that the proposed framework is well-suited for describing the mechanical behavior of sedimentary rocks with inherent anisotropy.

a)

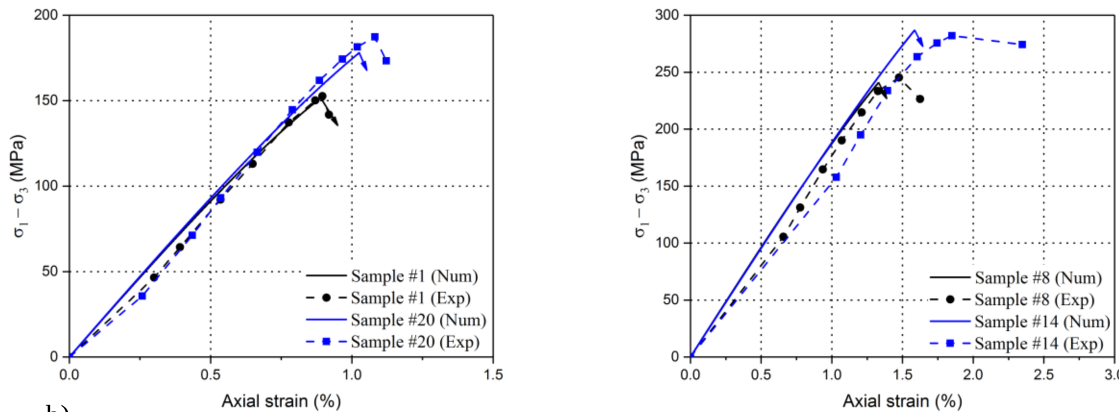

b)

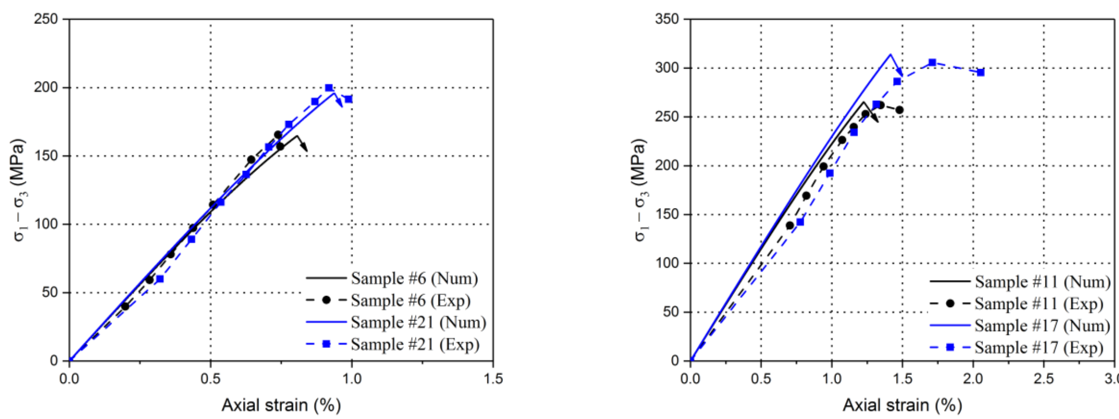

Fig. 2-8. Results of numerical simulations for samples with different volume fractions tested at various confining pressures; (a) samples cored vertical to the argillaceous partings, (b) samples cored along the argillaceous partings

CHAPTER 3

On quantification of equivalent permeability tensor in sparsely fractured rock masses [2]

The analysis presented here is based on Oda's concept of permeability tensor, the pipe network model (PNM), and a more sophisticated technique that incorporates the constitutive law with embedded discontinuity (CLED). The performance of each of these techniques is examined using different discrete fracture networks, with a focus on evaluating the eigenvalues and eigenvectors of the equivalent hydraulic conductivity tensor. The limitations of each of these techniques and their computational efficiency are analyzed, and a pragmatic approach for estimating the permeability tensor in fractured rock formations is proposed.

3.1 Methodologies for estimating the equivalent hydraulic conductivity tensor

3.1.1 Oda's concept of permeability tensor

Oda's concept of permeability tensor provides a fundamental approach to estimating the hydraulic conductivity of fractured rock masses. This approach considers a rock mass containing discontinuities as a homogeneous and anisotropic material and assumes that crack network can be approximated as an assembly of an equivalent set of parallel planar

[2] Note: This chapter includes substantial parts of the article published in the International Journal of Rock Mechanics and Mining Sciences:
P. Pakdel and S. Pietruszczak, On quantification of equivalent permeability tensor in sparsely fractured rock masses, *Int. J. Rock Mech. Min. Sci.*, vol. 178, p. 105735, 2024. https://doi.org/10.1016/j.ijrmms.2024.105735

surfaces. One crucial postulate in Oda's approach is that all head losses at intersections of the joints are assumed to be negligible, which implies that the fluid could flow seamlessly through the network of joints without additional resistance.

The problem is formulated by assuming that the flow through the fractured rock mass is governed by Darcy's law, which relates the apparent seepage velocity to the hydraulic gradient, i.e.

$$v_i = -k_{ij}\frac{\partial h}{\partial x_j} = k_{ij}\,J_j \tag{3.1}$$

In the above expression, v_i and k_{ij} represent the apparent seepage velocity and the hydraulic conductivity tensor, respectively, J_i is the hydraulic gradient, and h represents the total head. The formulation assumes that only the cracks provide conductive channels for fluid flow while the rock matrix itself is impervious. The flow velocity is assessed by taking an average over the referential volume of the flow domain (V), i.e.

$$v_i = \frac{1}{V}\int_{V^{(f)}} v_i^{(f)}\,\mathrm{d}V^{(f)} \tag{3.2}$$

where $v_i^{(f)}$ is the velocity of fluid within the fracture and $V^{(f)}$ is the volume of fractures. In the original approach [44], the fractures are considered as penny-shaped, having the diameter *r* and aperture t_D. Their orientation is defined by unit normal vectors n_i contained within the solid angle Ω corresponding to the surface of a unit sphere. In order to define the problem, the probability density function $E(n_i, r, t_D)$ is introduced such that $2E(n_i, r, t_D)d\Omega\; dr\; dt_D$ gives the probability of (n_i, r, t_D) fractures inside a differential angle $d\Omega$ around n_i. Thus, the fracture volume $\mathrm{d}V^{(f)}$ is given by

$$\mathrm{d}V^{(f)} = \frac{\pi r^2 t_D}{4} dN = \frac{\pi m^{(V)}}{2} r^2 t_D E(n_i, r, t) d\Omega \; dr \; dt_D \tag{3.3}$$

where dN is the number of fractures whose centers are located inside $\mathrm{d}V^{(f)}$ and $m^{(V)}$ is the total number of fractures. The local flow velocity within the fractures is approximated using the standard power law [65], which assumes laminar flow, i.e.

$$v_i^{(f)} = \lambda \frac{g}{\upsilon} \; t_D^2 \, J_i^{(f)}; \qquad J_i^{(f)} = (\delta_{ij} - n_i n_j) J_i \tag{3.4}$$

Here, g and υ are the gravitational acceleration and kinematic viscosity, respectively, $J_i^{(f)}$ is a component of J_i projected on (n_i, r, t_D) fracture, and λ is a dimensionless constant, which for fractures extending indefinitely assumes the value of 1/12. Substituting now eqs. 3.3 and 3-4 in eq. 3.2 leads to

$$\begin{aligned} v_i &= \frac{1}{V} \int_{V^{(c)}} v_i^{(f)} \, dV^{(f)} \\ &= \lambda \frac{g}{\upsilon} \frac{\pi \rho}{4} [\int_0^\infty \int_0^\infty \int_\Omega r^2 \; t_D^3 \left(\delta_{ij} - n_i n_j\right) E(n, r, t_D) d\Omega \; dr \; dt_D] J_i \end{aligned} \tag{3.5}$$

in which $\rho = m^{(v)}/V$ denotes the volume density of fractures. The equivalent hydraulic conductivity tensor is determined by comparing eqs. 3.5 and 3.1, so that

$$k_{ij} = \lambda \frac{g}{\upsilon} (P_{kk} \delta_{ij} - P_{ij}) \tag{3.6}$$

$$P_{ij} = \frac{\pi \rho}{4} \iiint r^2 \; t_D^3 \; n_i n_j E(n, r, t_D) d\Omega \; dr \; dt_D \tag{3.7}$$

Here, P_{ij} is a symmetric second order tensor (so-called crack tensor) whose components are a function of the geometry of fractures, i.e. size, shape, aperture, and orientation.

Note that in the case when the hydraulic conductivity of intact material cannot be neglected, eq. 3-2 becomes

$$v_i = \frac{1}{V}\int_V v_i \, \mathrm{d}V, \qquad \bar{v}_i = \frac{1}{V}\left(\int_{V^{(m)}} v_i^{(m)} \, \mathrm{d}V^{(m)} + \int_{V^{(f)}} v_i^{(f)} \, \mathrm{d}V^{(f)} \right) \tag{3.8}$$

which leads to

$$v_i = (k_{\mathrm{i}j}^{(m)} + k_{ij}) J_j \tag{3.9}$$

where the superscript m stands for matrix, i.e. intact material. Note that the fractures have negligible volume, so that the volume of the matrix $V^{(m)}$ may be approximated as being equal to V.

3.1.2 Pipe Network Model (PNM)

The pipe network model is a simple and pragmatic approach that has been employed in many different areas, including fluid flow in rock fractures [cf. ref. 66]. In the case of a discrete fracture system, the pipes (or flow channels) are viewed as a set of parallel plates of a given aperture, which is considered as uniform along the fracture. The intact rock is typically assumed to be impervious, so that fractures are the only paths for fluid transport. The fluid is considered as incompressible and the flow within fracture zone is assumed to be laminar, so that the fracture's conductivity is evaluated using again a standard power law. In a 2D flow model, fractures are discretized into line segments (of unit depth), each associated with two end nodes (i, j). A pipe segment with a length of l has a flow rate of

$$v_{(i,j)} = k_{(i,j)}\, J_{(i,j)} \qquad 3.10$$

where $J_{(i,j)} = (p_{(i)} - p_{(j)})\,/l$ is the hydraulic gradient between nodes i and j, while $p_{(i)}$ and $p_{(j)}$ are the corresponding pressure heads. The hydraulic conductivity coefficient for each pipe is estimated again based on the quadratic form

$$k_{(i,j)} = g\, t_D^2/12v \qquad 3.11$$

Here, t_d is the fracture aperture, while g and v are the gravitational acceleration and kinematic viscosity (typically $10^{-6}\, m^2/s$), respectively.

The quantity of flow between two connected nodes is given by

$$q_{(i,j)} = C_{(i,j)}(p_{(i)} - p_{(j)}), \qquad C_{(i,j)} = g\, t_D^2\, b/12vl \qquad 3.12$$

where b represents the fracture width, which is set to 1 for 2D simulations. The operator $C_{(i,j)}$ is the conductance of the pipe segment between nodes i and j, and it's directly related to the aperture's geometry.

The conservation of flux at each node can be expressed as

$$\sum_{i=1}^{n} q_{(i,j)} = 0 \qquad 3.13$$

where n is the number of neighboring nodes connected to node j. The above statement is illustrated in Fig. 3-1, where the conservation of flux at node #1 requires

$$q_{12} + q_{13} + q_{14} + q_{15} = 0 \tag{3.14}$$

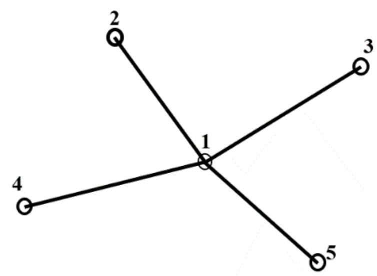

Fig. 3-1. An example of an interconnected node

Substituting eq. 3.12 into eq. 3.13, yields

$$p_{(j)} = \sum_{i=1}^{n} C_{(i,j)} p_{(i)} \Big/ \sum_{i=1}^{n} C_{(i,j)} \tag{3.15}$$

where $p_{(j)}$ is the pressure head at node j. It should be noted that the number of connected nodes (n) varies between 2 and 4 [cf. ref. 50].

The presence of fractures that do not contribute significantly to the flow can introduce inaccuracies. Therefore, the graph theory algorithm is used to identify and remove these fractures before hydraulic equations are solved. The first step in this algorithm is to identify the intersections of fractures, which defines the connectivity of the network. Two primary categories of inactive fractures include (*i*) isolated fractures, which are defined as those having no intersections or lack of connection to the boundaries of the domain, and (*ii*) dead-end fractures, i.e. those ending at a single node without connecting to other fractures. It should be noted that boundary edges are also treated as fractures in the analysis.

To initiate the process, all intersections between fractures and boundary edges are found, and this information is stored in a matrix that monitors the connectivity of the network. In this step, fractures that are not intersected and segments with free end nodes (i.e., nodes not connected to boundaries or other fractures) are automatically eliminated. Then, fractures with two end nodes that are not tied to the boundary are found and also eliminated. After the removal of all fractures that do not contribute to the fluid flow, the matrix containing all remaining nodes and fracture segments is updated.

Since the removal of isolated and dead-end fractures can lead to the creation of new ones, an iterative process is applied. The network is re-examined to detect additional fractures that have become isolated or have only two disconnected end nodes. The final step involves detecting and eliminating any groups of fractures that remain disconnected from the boundary edges. The resulting DFN consists exclusively of fractures that maintain at least two intersections with other fractures or with the boundary edges. Thus, only hydraulically significant pathways are retained in the network.

There are two types of nodes in PNM, i.e. boundary nodes and inner nodes. The former consist of inlet nodes, outlet nodes, and secondary boundary nodes. The inlet node is the beginning point of a flow, while the outlet node is the endpoint of the flow. Thus, the flow begins at inlet nodes, passes through internal nodes, and arrives at the outlet nodes. The secondary boundary nodes are generated by intersecting fractures with boundary edges. The pressure heads in inlet and outlet nodes are known, and the pressure heads in the secondary nodes can be estimated by interpolating the heads of inlet and outlet nodes based on their distance from boundaries.

In the numerical process, the pressure heads at the inner nodes remain unknown and must be determined using eq 3.15. For the entire network system, a matrix equation is established to describe the discretized conservation equations of all nodes in a fracture network. This is written in the form

$$[H]_{(m\times m)}\,\{p\}_{(m\times 1)} = \{B\}_{(m\times 1)} \qquad 3.16$$

where

- m is the number of nodes
- [H] is the global conductance matrix. The diagonal components of [H] are given by $\sum_{i=1}^{n} C_{ij}$. , while the off-diagonal components H_{jk} are equal to $-C_{ij}$ if node j is connected to node k, and zero otherwise.
- $\{p\}$ is the matrix of unknown pressure heads, where p_j represents the pressure head at node j.
- $\{B\}$ are the products of $C_{(i,j)}$ and the pressure head at the boundary nodes $p_{(j)}^{(b)}$. If node j is not connected to a boundary, B_j is set to zero.

Eq. 3.16 can be solved by either direct or iterative methods. After the nodal pressure heads are calculated, the flow rate in each pipe can be determined according to eq. 3.12. For the entire flow domain, the coefficient of hydraulic conductivity in the direction of hydraulic gradient is obtained as the ratio of the total rate of flow from fractures intersecting the outflow boundary and the imposed hydraulic gradient.

3.1.3 Constitutive law with embedded discontinuity (CLED)

The approach incorporating the constitutive law with embedded discontinuity (CLED) was first proposed in the early 1980s (e.g., refs. [67-68]). Initially, the primary focus of CLED was on capturing the mechanical behavior of single-phase solids, particularly on modeling the propagation of damage in brittle and frictional materials. This framework was later enhanced to deal with the discrete tracing of cracks and was applied to a broad range of problems in both structural mechanics and geomechanics. Over time, the scope of this approach was expanded to encompass more complex multi-physics interactions, particularly the coupling between mechanical deformation and fluid flow [54, 69]. This advancement allows for a more realistic representation of how fractures and their geometry affect the permeability in naturally fractured geomaterials.

In terms of hydraulic response, the formulation employs a modified form of Darcy's law in which the hydraulic conductivity in the region containing an embedded discrete fracture is assessed through volume averaging of gradient operators of discontinuous fields. The methodology involves imposing a weak discontinuity in fluid pressure within the considered referential volume. By enforcing admissible constraints in the flow regime, an average hydraulic conductivity operator is established, whose definition incorporates a length scale parameter χ. The latter represents the ratio of the surface area of fracture to the volume of the referential domain. The hydraulic conductivity tensor is then defined, whose value is affected by both the permeability of the intact rock and that of the embedded fracture. Thus, the conductivity in fractured regions is influenced by fracture aperture, orientation, and connectivity, all of which are integrated into the model through the length-scale parameter and hydraulic constraint operators. The homogenized constitutive relation governing the fluid flow at the macroscale takes the form [54].

$$v_i = \frac{1}{\rho_f g} k_{ij}\left(-p_{,j} + \rho_f g_j\right) ;$$
$$k_{ij} = \left((1-\chi t_D)k_{iq}^{(m)} + \chi t_D\, k_{ip}^{(f)} c_{pq}\right)\left[\delta_{qj} + \chi t_D\,(c_{qj} - \delta_{qj})\right]^{-1} \qquad 3.17$$

Here, $k_{ij}^{(m)}$ and $k_{ij}^{(f)}$ are the hydraulic conductivity tensors in the matrix and fractured regions, respectively, and c_{ij} is an operator that defines the hydraulic constraints

$$c_{ij} = \begin{bmatrix} t_i \\ k_{qi}^{(f)} n_q \\ s_i \end{bmatrix}^{-1} \begin{bmatrix} t_j \\ k_{pj}^{(m)} n_p \\ s_j \end{bmatrix} \qquad 3.18$$

where n_i stands again for the unit normal to the fracture and t_i and s_i are the base vectors along the discontinuity. The above enhanced form of Darcy's law, eq. 3.17 captures the transition from matrix-dominated to fracture-dominated flow within a single constitutive equation. The approach has the advantage of being both accurate and computationally very efficient since it can be used in standard finite element analysis without the need for any additional degrees of freedom. This makes it particularly well-suited for large-scale geomechanical problems where a fully explicit representation of fractures would be impractical.

3.2 Numerical study involving deterministic fracture networks

3.2.1 Discrete Fracture Network (DFN) #1

Consider first a sparsely fractured domain containing a number of elongated fractures, as shown in Fig. 3-2. The flow region has a size of 10 x 10m, and the boundary conditions are defined in terms of fluid pressure. The vertical boundaries are subjected to constant pressures of p = 20 MPa and p = 10 MPa, respectively, while a linear pressure variation is imposed along the horizontal boundaries. Hence, in a homogeneous material, the hydraulic gradient is coaxial with the horizontal axis, which implies a horizontal flow. In the presence of a discrete fracture network (DFN), however, the flow pattern is significantly more complex and is strongly affected by the spacing and orientation of the fractures, which play a dominant role in redirecting the fluid pathways.

Since the fracture geometry is predefined here, Oda's approach (eq. 3.7) allows the integral form to be replaced by a discrete summation, which enables a more straightforward computation of the hydraulic conductivity tensor. For a 2D fracture network, the components of the crack tensor can be expressed as (cf. refs. [44, 49]).

$$P_{ij} = \left(\sum_{k=1}^{m^{(V)}} t_D^3 \, L_{(k)} n_i n_j\right)/A \qquad 3.19$$

where k represents the kth fracture among the total of $m^{(V)}$ fractures, L is the length of each fracture, t_D is the aperture size, n_i are the components of the unit normal vector, and A is the total area of the considered flow domain.

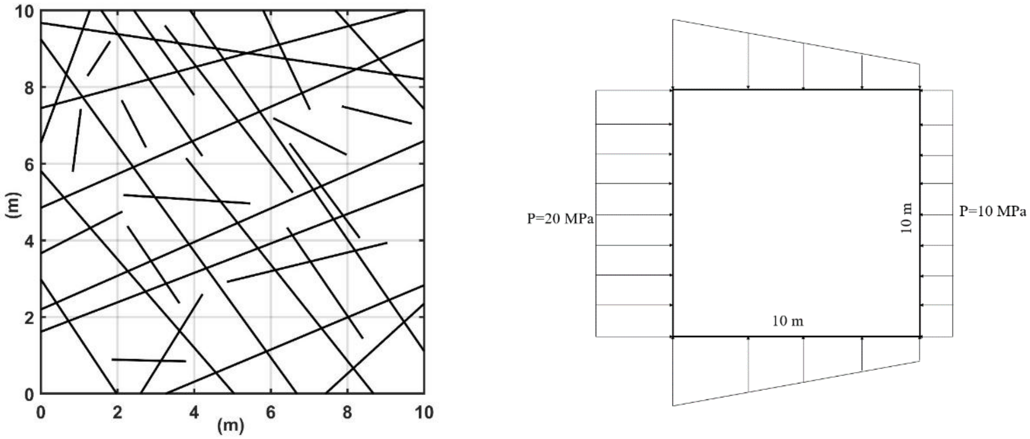

Fig. 3-2. Geometry of the discrete fracture network #1 and the boundary conditions for the flow

For the above fracture network (Fig. 3-2), the matrix is considered as impermeable, and therefore the fluid movement is restricted only to the fracture system. The fracture aperture is taken as 0.1 mm, and the kinematic viscosity of the fluid at room temperature is assumed to be $10^{-6}\,m^2/s$. Given the above parameters, as well as the geometry of DFN, the components of the hydraulic conductivity tensor, eq. 3.6, were obtained as

$$k_{ij} = \begin{bmatrix} 5.867 \times 10^{-7} & 1.174 \times 10^{-7} \\ 1.174 \times 10^{-7} & 8.806 \times 10^{-7} \end{bmatrix}$$

which corresponds to $k_1 = 9.22 \times 10^{-7}$ m/s, k_2 =5.45$\times 10^{-7}$ m/s while the orientation of the major principal direction is equal to 70.7° with respect to the horizontal axis.

For the analysis based on the pipe network model, the first step was to trim the DFN using the graph theory algorithm [29]. As mentioned earlier, the objective was to detect and remove isolated and dead-end fractures. These types of fractures, while present in the rock mass, do not play a significant role in enhancing the overall permeability of the domain and could introduce inaccuracies if included in the computational analysis. Fig. 3-3 shows the trimmed DFN, along with the corresponding sets of nodes and edges. The modified network has 86 nodes and 115 edges.

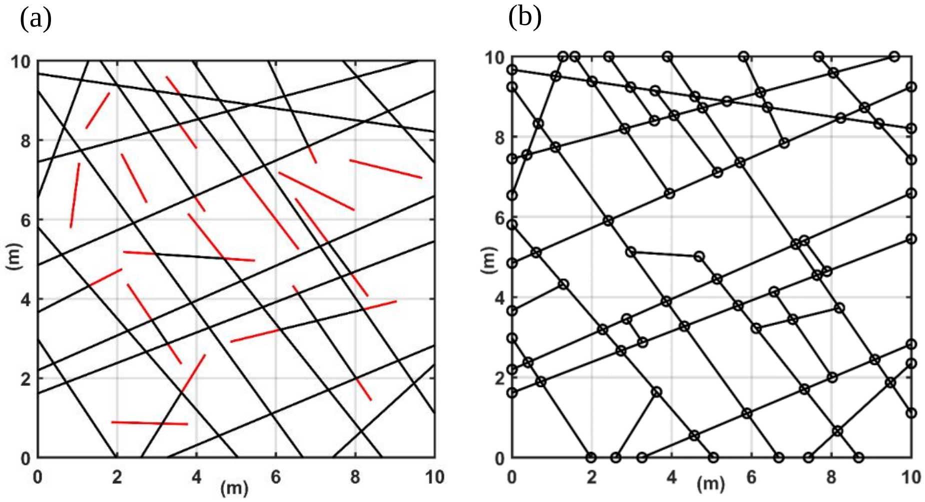

Fig. 3-3. (a) The trimmed fracture network (removed segments marked in red), (b) Nodes and edges of the trimmed DFN

The analysis was carried out by solving the set of algebraic eq. 3-16. The numerical code was written in MATLAB R2021b. Fig. 3-4 shows the results pertaining to the fluid pressure distribution across the trimmed discrete fracture network (DFN). The pressure is within the range of 10-20 MPa, which is consistent with the imposed boundary conditions.

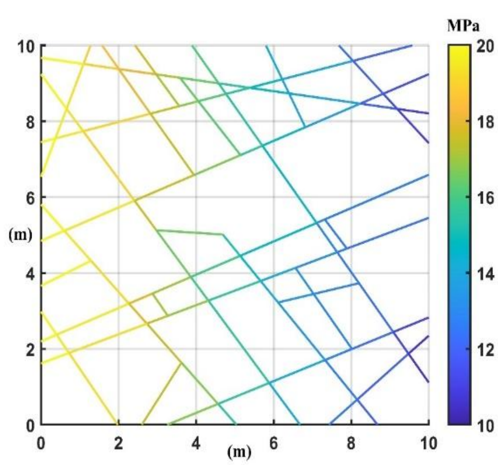

Fig. 3-4. The distribution of fluid pressure calculated by the pipe network model

The assessment of the principal values of the hydraulic conductivity tensor and their corresponding orientations can be carried out by constructing a two-dimensional conductivity ellipse or, in the case of a three-dimensional system, an ellipsoid. Such a geometric representation provides a visual and mathematical means to quantify the directional variations in hydraulic conductivity within the fractured domain. The specification of this measure requires the evaluation of the conductivity coefficient in the direction of the imposed hydraulic gradient for different orientations of the fracture network. As shown in ref. [70], if x_1 and x_2-axes are along the principal directions, then the hydraulic conductivity ellipse is described by the equation

$$\frac{x_1^2}{\left(1/\sqrt{k_1}\right)^2} + \frac{x_2^2}{\left(1/\sqrt{k_2}\right)^2} = 1 \qquad 3.20$$

In this representation, the conductivity in an arbitrary direction α is given by $1/\sqrt{k_\alpha}$. Thus, the minor and major axes have a length of $1/\sqrt{k_2}$ and $1/\sqrt{k_1}$, respectively, where k_1 and k_2 are the principal values of hydraulic conductivity and x_1 and x_2 are aligned with the principal directions.

As mentioned earlier, for DFN rotated by an angle α, the coefficient of hydraulic conductivity in the direction of the hydraulic gradient is obtained as the ratio of the total rate of flow from fractures intersecting the outflow boundary and the imposed hydraulic gradient. Figs. 3-5b to 3-5d show the rotated fracture network at α = 60°, 105° and 165°, respectively. The spatial distribution of hydraulic conductivity and its best-fit approximation based on eq. 3.15, are shown in Fig. 3-6. For the given set of material parameters, the calculated principal hydraulic conductivities are k_1 =7.28×10^{-7} m/s,

k_2 =3.53×10^{-7} m/s, while the orientation of the major principal direction is 169.6° with respect to horizontal axis.

It is evident that the results obtained by using this approach are markedly different from those obtained by using Oda's approach. This discrepancy stems primarily from the fundamental assumptions underlying Oda's method, which considers all fractures as active flow pathways without explicitly accounting for their connectivity. Furthermore, Oda's formulation models the fracture network using statistical distributions of fracture aperture, size, and orientation rather than explicitly incorporating the deterministic geometric configuration of discrete fractures. While this statistical approach provides a rapid and computationally efficient means of estimating permeability, its accuracy is low in cases when fracture connectivity and spatial arrangement play a dominant role in controlling the flow behavior.

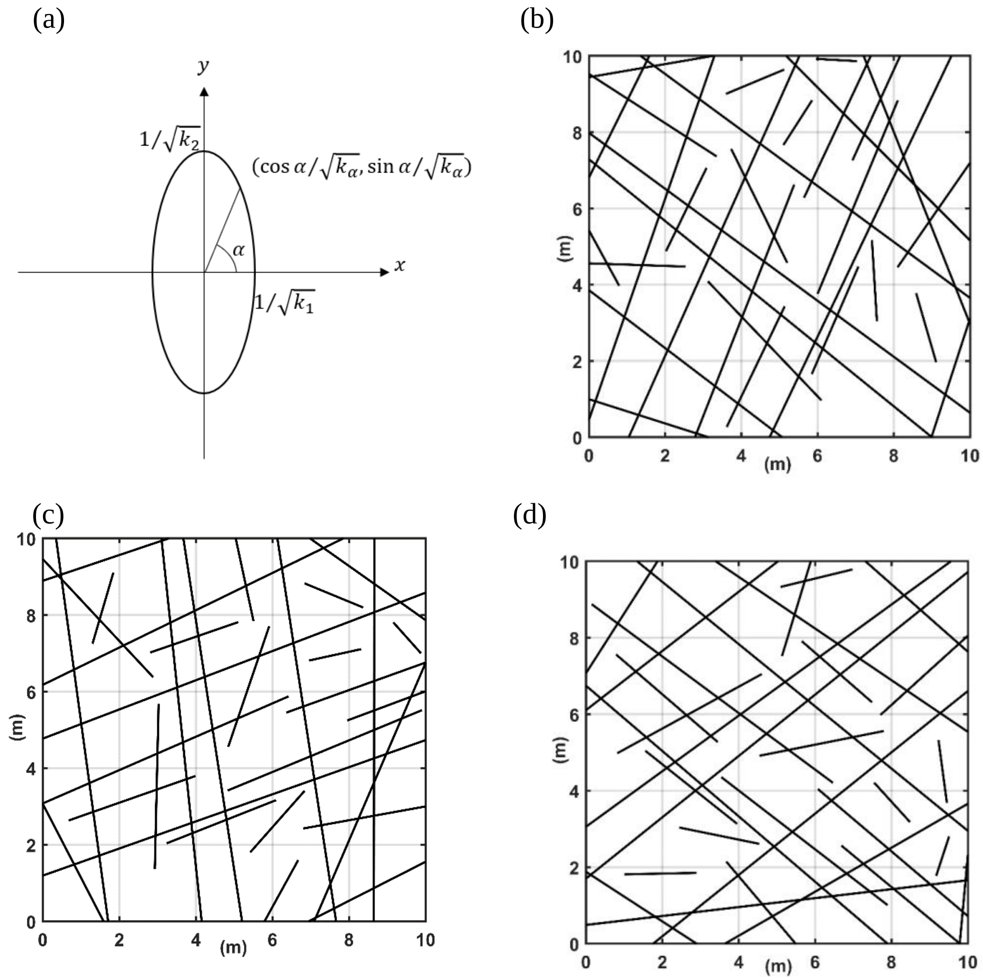

Fig. 3-5. (a) The hydraulic conductivity ellipse in the principal material system, (b), (c), (d) Rotated fracture network at α = 60°, 105° and 165°

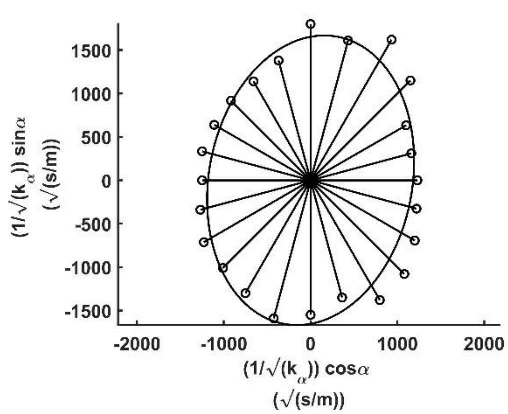

Fig. 3-6. Fitted hydraulic permeability ellipse for the pipe network model

Among all methodologies discussed in Section 3-1, the constitutive law with embedded discontinuity (CLED) provides the most reliable assessment of equivalent hydraulic conductivity. As demonstrated in ref. [54], this approach can capture the flow pattern in a very accurate way, accounting for properties of both the intact domain and the pre-existing fractures. Also, the CLED approach can integrate mechanical and hydraulic aspects within the same conceptual framework [67], which allows for tracing the evolution of fracture aperture and its impact on permeability changes under varying stress conditions.

The analysis conducted in this study employed an unstructured mesh that consisted of 2500 four-noded rectangular elements, as shown in Fig. 3-7. The elements containing embedded fractures were assigned homogenized hydraulic properties, following the formulation provided in eq. 3-17. These fractured elements are highlighted in yellow in Fig. 3-7.

Again, the assessment of equivalent hydraulic conductivity required a set of simulations at different orientations of the sample relative to the imposed direction of the hydraulic gradient (Fig. 3-2). The primary results of these simulations are presented in Figs. 3-8 and 3-9. Fig. 3-8a shows the distribution of pore pressure within the analyzed domain, while Fig. 3-8b provides a schematic diagram of the velocity field. The latter clearly illustrates how the fluid is channeled through the interconnected fracture network. Both sets of results presented here correspond to the original geometry (Fig. 3-2) without any rotation. It is evident that the pore pressure distribution obtained from the CLED-based simulations is qualitatively similar to that derived from the trimmed discrete fracture network analyzed by the pipe network model (Fig. 3-4). Also, it is apparent that velocity in isolated and dead-end fractures, as predicted in CLED approach is indeed negligible, which supports the validity of the trimming approach employed in PNM and confirms that these fractures have minimal impact on the overall fluid transport within the domain.

To quantify the anisotropic hydraulic properties of the fractured rock mass, the eigenvectors and eigenvalues of the hydraulic conductivity tensor were determined using the same set of rotated geometries as depicted in Figs. 3-5 b, c, and d. The obtained spatial distribution of the conductivity coefficient, together with the best-fit approximation, is shown in Fig. 3-9. In this case, the predicted eigenvalues of the equivalent hydraulic conductivity operator are $k_1 = 4.28$×10-7 m/s, k_2 =3.03×10-7 m/s, while the orientation of the major principal direction is equal to 155.1°.

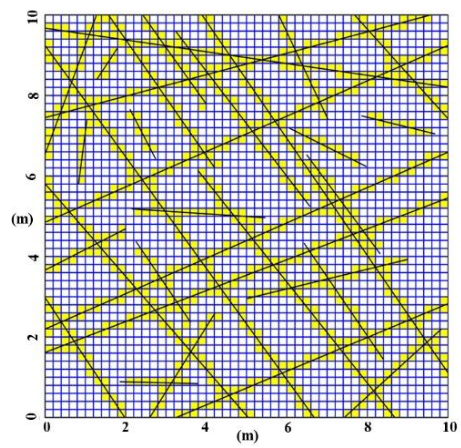

Fig. 3-7. Finite element discretization for the CLED approach (elements with embedded fractures are shown in yellow)

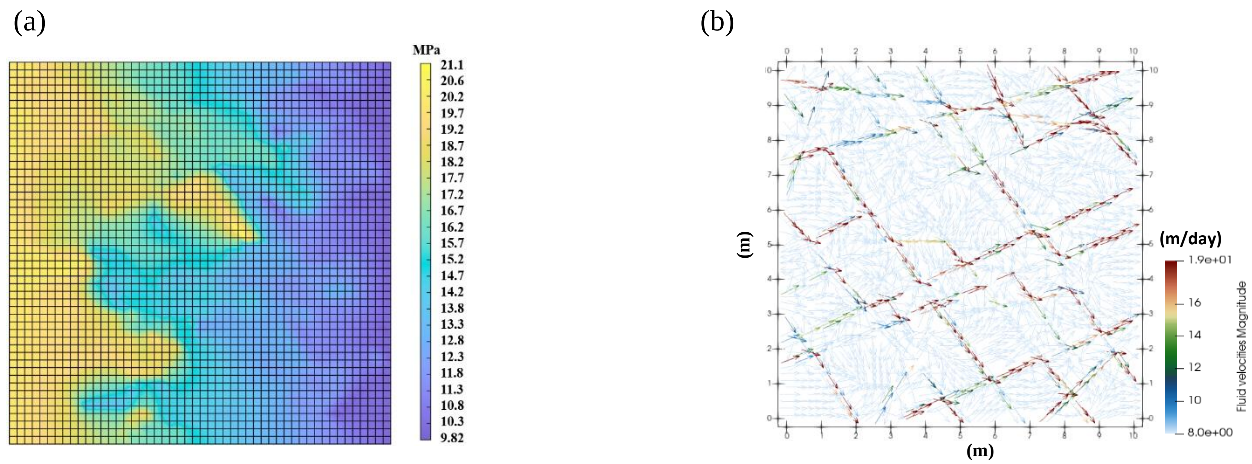

Fig. 3-8. (a) Distribution of pore fluid pressure and (b) the velocity field inside the considered domain

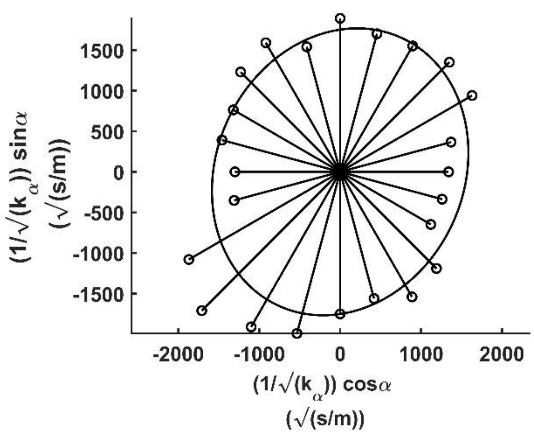

Fig. 3-9. Fitted hydraulic conductivity ellipse for the CLED approach

By examining the results obtained from the different methodologies, it becomes evident that the predictions of the CLED approach, which is regarded as the most reliable method in this study, exhibit much closer agreement with those obtained using the pipe network model (PNM) than Oda’s model. In particular, the principal directions of hydraulic conductivity operator are fairly consistent in CLED and PNM approach, cf. Fig. 3-10a. The reason lies in the fundamental characteristics of both methods, i.e. they explicitly account for fracture connectivity, which is a critical factor in assessing the overall permeability of the fractured rock mass. As mentioned earlier, Oda's permeability tensor approach assumes all fractures to be interconnected, which tends to overestimate permeability in a sparsely fractured domain.

One of the key advantages of the CLED approach is that no a priori assumptions need to be made regarding the flow pathways, as the flow velocity field is a part of the solution. This is particularly important when conducting coupled hydro-mechanical simulations, where changes in connectivity may occur due to the propagation of existing fractures and the onset of new ones. The pre-evaluation of flow paths in PNM is rather intuitive; hence, the trimming of the fracture network may not be accurate. This input-preprocessing method is still effective in refining the network but adds a lot of uncertainties, especially for irregularly spaced and complex fractures. As a result, some discrepancies remain between the PNM and CLED solutions, especially in the estimated principal values of the hydraulic conductivity tensor.

Given these observations, a pragmatic and computationally efficient strategy for estimating the equivalent hydraulic conductivity tensor would be to adopt a hybrid approach. In this case, the eigenvectors may be obtained based on PNM approach. The eigenvalues could then be assessed by examining the flow pattern in the principal material directions by means of the CLED approach, i.e. by incorporating the constitutive law with embedded discontinuity. This is a simple and efficient way of getting reliable estimates for the equivalent hydraulic conductivity in the presence of discontinuities. The validity of this proposed approach is illustrated in Fig. 3-10b, which compares the conductivity ellipse obtained through this approximate procedure vs the exact CLED solution.

(a) (b)

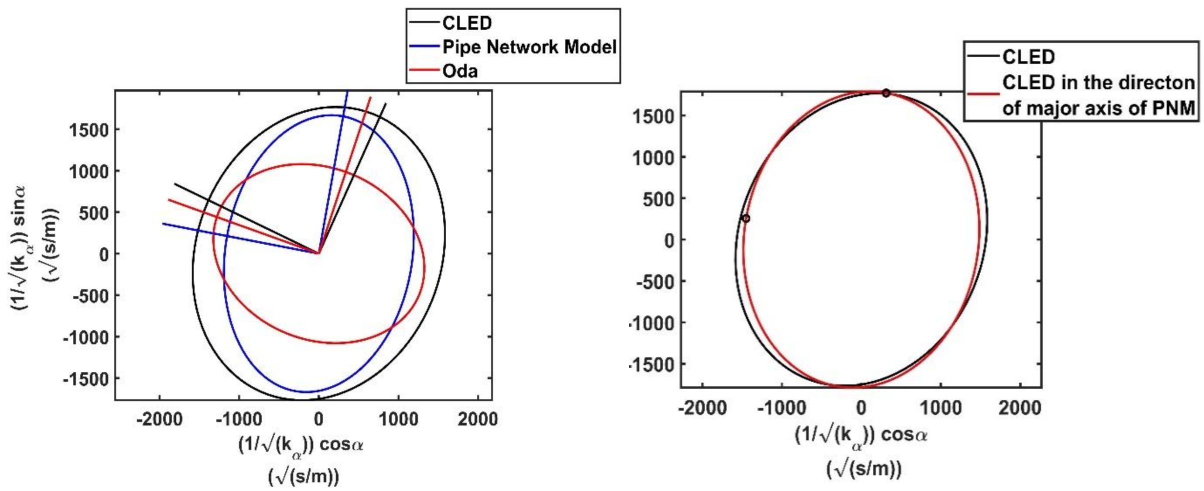

Fig. 3-10. (a) Comparison of the predicted hydraulic conductivity ellipse for the three methods used; (b) conductivity ellipse for CLED approach incorporating the principal directions based on PNM

3.2.2 Discrete Fracture Network (DFN) #2

The second discrete fracture network that has been examined in this paper is shown in Fig. 3-11. The main objective of investigating this network was to confirm the general findings previously reported and to provide a parametric study of the effect of permeability of the intact rock and the fracture aperture. Note that both these variables play an important role in defining the flow characteristics of fractured rock masses, so that their impact also needs to be quantified. The boundary conditions, as well as the material and geometric parameters employed here, are the same as those used in the previous example. The latter also allows for a direct comparison between the two DFNs, highlighting any variations in hydraulic behavior that could be attributed to differences in fracture density, orientation, and connectivity.

For the analysis based on the pipe-network model, the DFN was again trimmed by eliminating the dead ends and isolated fractures, as illustrated in Fig.3-12. In order to perform the CLED simulations, the same unstructured finite element mesh was used as that shown in Fig. 3-7, which had a total of 2500 four-noded rectangular elements.

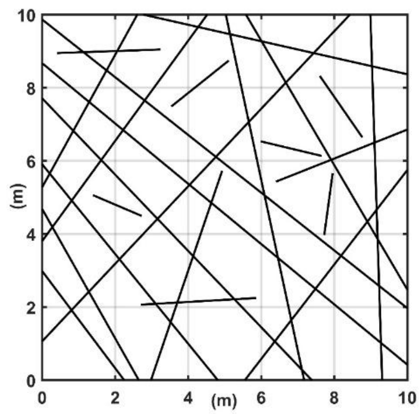

Fig. 3-11. Geometry of the discrete fracture network #2

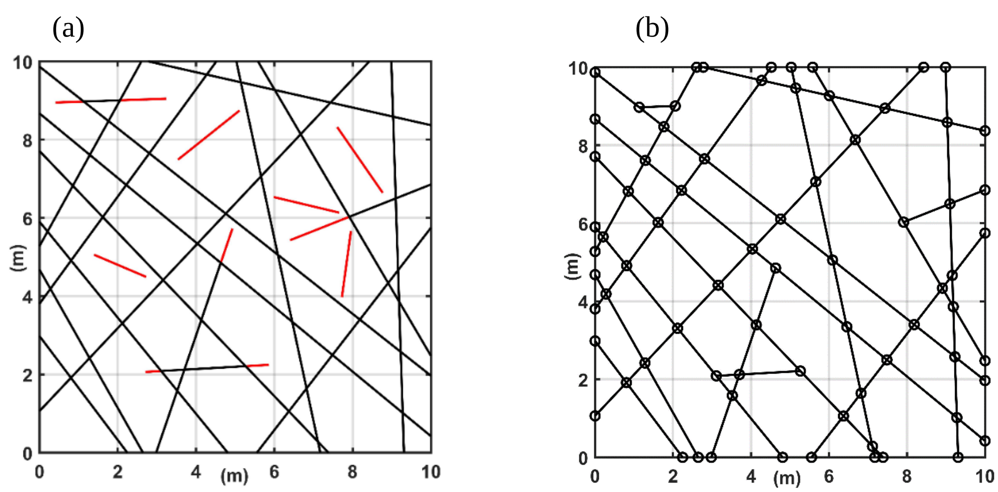

Fig. 3-12. (a) The trimmed fracture network for PNM analysis (removed segments marked in red); (b) nodes and edges of the trimmed DFN

Fig. 3-13 shows the best-fit approximations to the hydraulic conductivity ellipse for both methodologies. In this case, the principal values and the orientation of major principal axes

β , were determined as

Pipe network model: $k_1 = 6.94 \times 10^{-7}\ \mathrm{m/s}$, $k_2 = 3.02 \times 10^{-7}\ \mathrm{m/s}$, β=113.8°

CLED approach: $k_1 = 5.57 \times 10^{-7}\ \mathrm{m/s}$, $k_2 = 2.75 \times 10^{-7}\ \mathrm{m/s}$, β=109.2°

For Oda's approach, once again, the principal values of permeability are overestimated, and the predicted orientation of the major principal axis β is substantially different, i.e.

Oda approach: $k_1 = 8.43 \times 10^{-7}\ \mathrm{m/s}$, $k_2 = 5.075 \times 10^{-7}\ \mathrm{m/s}$, β=28.0°

The hydraulic conductivity ellipses for the three approaches are provided in Fig. 3-14a. In addition, Fig. 3-15b shows the solution for CLED approach incorporating the principal directions based on PNM. It is evident that the hybrid scheme proposed here gives sufficiently accurate results while reducing computational complexity.

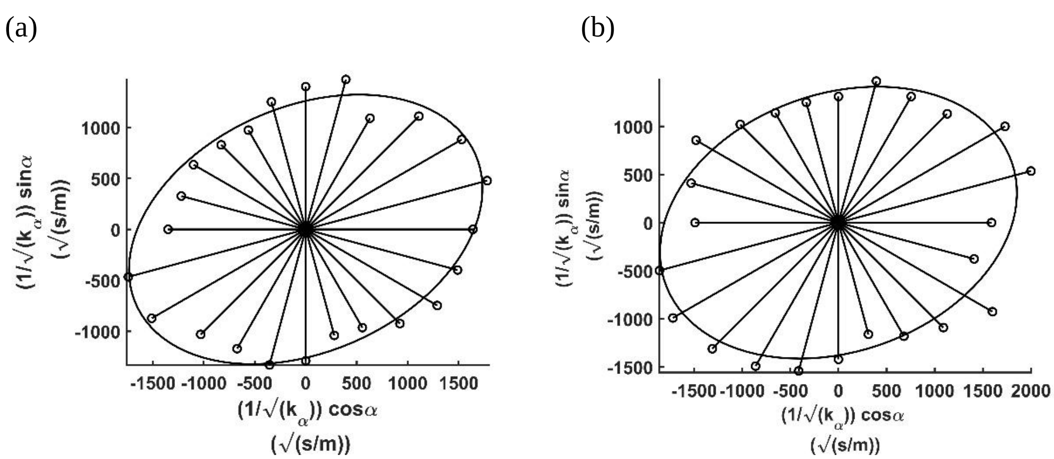

Fig. 3-13. Fitted hydraulic conductivity ellipse for (a) PNM analysis and (b) CLED approach

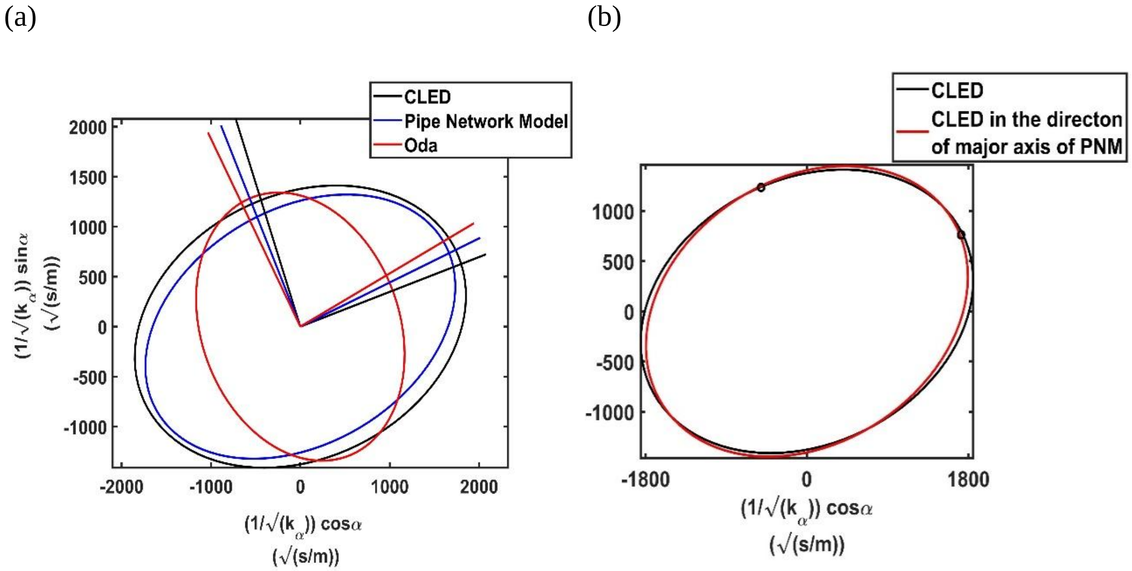

Fig. 3-14. (a) Hydraulic conductivity ellipse for the three methods used; (b) conductivity ellipse for CLED approach incorporating the principal directions based on PNM

3.2.3 Assessment of the influence of permeability of intact rock and the fracture aperture

The last stage of analysis involved a parametric study examining the influence of properties of constituent materials on the predicted equivalent hydraulic conductivity. The study has been conducted using constitutive law with embedded discontinuity (CLED). It is noted that in several geological formations, the fluid movement is not solely through fractures, but permeation occurs through the intact rock mass, albeit at a lower rate. Capturing this effect is of importance for certain types of rocks, especially those with higher porosity. Thus, the first part of the parametric study is focused on determining the influence of matrix permeability.

Fig. 3-15 shows the comparison of the results corresponding to an impervious intact rock and the one with a hydraulic conductivity of 4.0×10^{-8} m/s. For the latter case, the principal values and principal direction β of hydraulic conductivity were determined as

CLED approach (permeable matrix): $k_1 = 7.41 \times 10^{-7}$ m/s, $k_2 = 3.67 \times 10^{-7}$m/s, β=113°

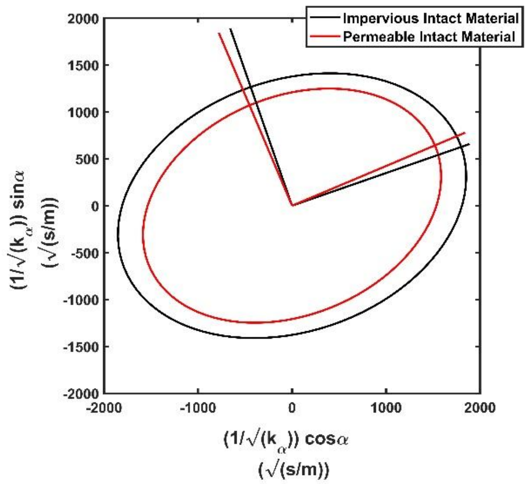

Fig. 3-15. Comparison of the hydraulic conductivity ellipse for an impervious and permeable intact rock (CLED approach)

It is evident that the impact of matrix permeability is quite visible here, particularly in terms of the eigenvalues of the equivalent hydraulic conductivity operator.

It should be noted that the pipe network model (PNM) was not included in this part of the analysis. This is because, among the different methodologies used, the CLED approach is the only one capable of reliably incorporating the effects of matrix permeability. For the PNM approach, the accuracy of representing the flow through the intact domain by incorporating the concept of 'matrix pipes' is open to questions and has not been attempted here. It should also be mentioned that the hydraulic conductivity of intact rocks varies widely. For crystalline rocks, like granite, it is typically within the range between 10^{-11} and 10^{-12} m/s. The latter values are significantly lower than those assumed in the present study. This implies that for this type of rock, the matrix transmissivity will impact the macroscale properties only in cases when the fracture aperture is markedly less than 0.1mm, which is the value adopted in the example above.

In the second part of this investigation, the effect of fracture aperture was examined. The latter is the most critical variable that has a substantial impact on fluid transmissivity. Unlike matrix permeability, which remains relatively uniform across the intact rock, the fracture aperture can vary significantly due to geological processes, stress conditions, and mineral deposition. In order to assess its impact on the overall permeability of the rock mass, a series of numerical simulations was conducted using again the CLED approach. The analysis was carried out assuming the same constant matrix conductivity of 4.0×10^{-8} m/s and fracture aperture varying between 0.025 mm and 0.5 mm. The main results of the analysis are provided in Fig. 3-16 and Table 3-1. It is evident that the impact of the fracture aperture is very pronounced. For the considered range of fractures' thickness, the equivalent hydraulic conductivity increases by nearly four orders of magnitude. Since the aperture is assumed to be uniform throughout the domain, the principal directions of the permeability tensor remain the same. It is noted, however, that in the case of fracture networks occurring naturally, where aperture variation is spatially heterogeneous, the interaction of fracture geometry with the fluid flow would become more complex and would, in general, require more advanced coupled hydro-mechanical analysis.

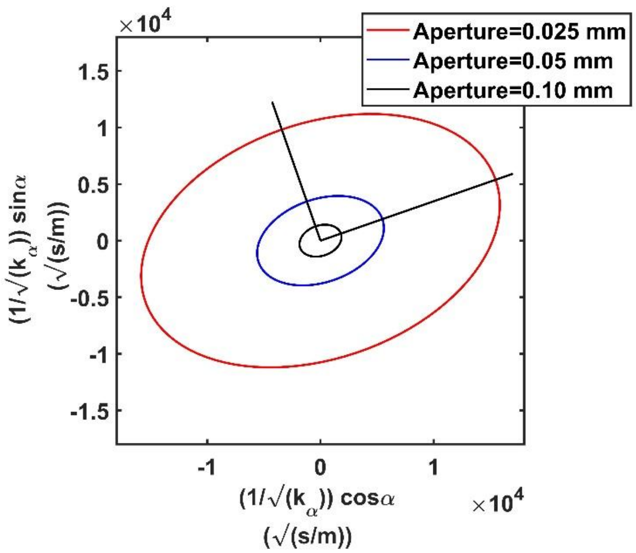

Fig. 3-16. Fitted hydraulic conductivity ellipses for different thicknesses of fractures

Table 3-1. The principal values of hydraulic conductivity tensor for different fracture apertures

Fractures' thickness	$k_1\ (m/s)$	$k_2\ (m/s)$
$t = 0.025\ \times 10^{-3}\ m$	0.093×10^{-7}	0.038×10^{-7}
$t = 0.05\ \times 10^{-3}\ m$	0.742×10^{-7}	0.298×10^{-7}
$t = 0.1\ \times 10^{-3}\ m$	5.57×10^{-7}	2.75×10^{-7}
$t = 0.3\ \times 10^{-3}\ m$	160×10^{-7}	64×10^{-7}
$t = 0.5\ \times 10^{-3}\ m$	742×10^{-7}	298×10^{-7}

The final aspect of this study concerns the scenario in which the rock mass contains two distinct families of fractures with different aperture sizes. In this case, two values of fracture thickness were chosen, viz. 0.1 mm and 0.4 mm. Fig. 3-17 shows the spatial distribution of these fracture families, while Fig. 3-18 presents the obtained hydraulic conductivity ellipse. The associated principal values and the orientation β of major principal axes are

Two sets of fractures' apertures: $k_1 = 24.9 \times 10^{-7}$ m/s, k_2 =11.9×10^{-7} m/s, β=85.31°

It is clear that in this case, not only the eigenvalues but also the principal directions of the equivalent hydraulic conductivity are affected. The latter stems from a strong interdependence of fracture transmissivity and the aperture, which is assumed to be governed by a power law.

Summarizing, the CLED approach appears to be the most robust methodology for incorporating the complex interactions between fracture aperture, matrix permeability, and hydraulic conductivity. Its ability to account for fracture connectivity as well as matrix flow makes it a reliable tool for estimating permeability in fractured rock mass.

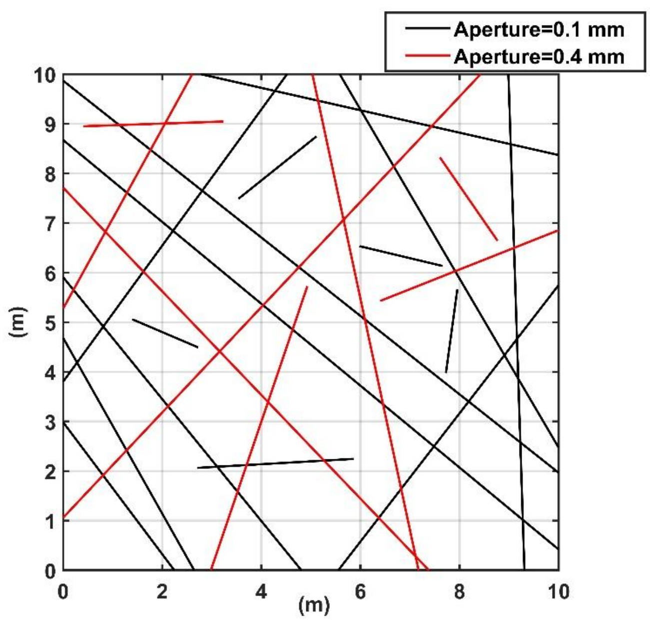

Fig. 3-17. The fracture network with two different sets of fractures' thickness

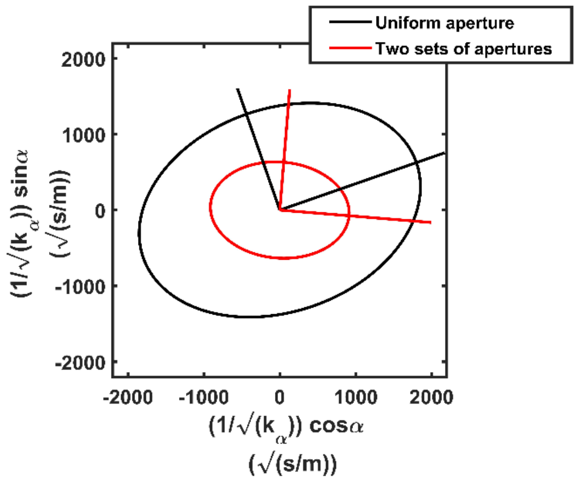

Fig. 3-18. Fitted hydraulic conductivity ellipse

CHAPTER 4

CONCLUSIONS AND RECOMMENDATIONS

4.1 Summary and Conclusions

The first part of this study focused on the description of mechanical properties of Cobourg limestone using a fabric-dependent approach. The framework incorporated the concept of mean intercept length as a quantitative measure of the rock's structural arrangement. The results showed that the Cobourg limestone may be considered as a transversely isotropic material, and its preferred direction is perpendicular to the argillaceous partings that are approximately parallel to the rock stratification.

To quantify the inherent anisotropy in the mechanical properties, the strength anisotropy parameter was introduced defined as a projection of the deviatoric part of the fabric tensor on the loading direction. Since for Cobourg limestone the preferred material direction is known in advance, no explicit information on the eigenvalues of the fabric tensor is required, which implies that no specific fabric measure needs to be explicitly employed. However, for a complex heterogeneous microstructure, a specific fabric descriptor needs to be incorporated in order to define the orientation of the material axes.

The study also examined the role of heterogeneity in determining the strength properties of Cobourg limestone. The conditions at failure were defined by invoking a hypothesis that the spatial distribution of strength is affected by the volume fraction of argillaceous facies.

A simplified linear dependence was used to specify the average value of strength anisotropy parameter as well as the bias in its distribution, which was largely due to a lack of actual experimental data correlating strength with fabric heterogeneity. An identification procedure was established to identify this function, using a 3D surface in the affined space of its arguments. The coefficients of the best-fit approximation were obtained by analyzing nearly twenty triaxial test results, in which the volume fraction of argillaceous partings in each specimen was estimated through digital image processing of binary surface images.

To validate the predictive abilities of the proposed framework, numerical analysis was conducted simulating the triaxial response of Cobourg limestone under different confining pressures, ranging from 10 MPa to 60 MPa. The analysis considered both horizontally and vertically cored samples to examine the anisotropic nature of the rock's deformation and the conditions at failure. The deformation characteristics were modeled using a plasticity formulation incorporating a deviatoric hardening to capture the path-dependent response of the material. It was found that, despite the inherent simplifications in the model that stem from limited information on the material fabric, the agreement with the experimental data was quite reasonable. The proposed formulation clearly has the ability to capture the key anisotropic features in strength and deformation characteristics, and thus could be useful in practical engineering applications.

Apart from the description of mechanical anisotropy in Cobourg limestone, this study was also focused on developing an adequate and efficient technique to evaluate equivalent hydraulic conductivity in fractured rock mass. Given the complex nature of fluid flow through fractured geomaterials, several different approaches were examined, and their suitability for capturing the anisotropic permeability behavior was assessed. The first approach that was considered was the notion of Oda's permeability tensor whose components are an explicit function of fractures' aperture, orientation and their spatial distribution. This approach is computationally efficient; however, it assumes that all fractures form a fully interconnected network and equally contribute to fluid flow. For sparsely fractured rock masses, this assumption is clearly not valid. As a result, this oversimplification produces considerable errors in predicting the principal values and principal directions of the hydraulic conductivity tensor, especially when fractures are not regularly distributed or do not form continuous pathways.

To overcome these limitations, the pipe network model (PNM) was examined. In this approach, the fractures are considered as flow channels, and their hydraulic conductivities are quantified using the graph theory algorithm. The primary advantage of this approach is that only those fractures that affect the overall permeability of the rock mass are taken into account, and therefore, the accuracy of estimation increases. One drawback of the PNM technique is that the intact material is usually regarded as impervious, which may not necessarily be the case in many natural geomaterials where the matrix permeability is not negligible.

Both the Oda permeability tensor approach and the pipe network model were implemented in a numerical study involving two deterministic fracture networks. For the PNM analysis, the volume of flow along the imposed hydraulic gradient was evaluated for different orientations of the fracture network and the components of the equivalent hydraulic conductivity tensor were estimated. While Oda's model significantly overestimated the permeability, the pipe network model provided a more precise assessment of the flow paths. As a result, there was a noticeable difference in the predicted eigenvalues and eigenvectors of the hydraulic conductivity operator.

In order to enhance the accuracy of permeability estimations, a more advanced method that employs a constitutive law with embedded discontinuity (CLED) was implemented. The formulation incorporates an augmented form of Darcy's law in which the hydraulic conductivity in the region containing embedded fractures is assessed through volume averaging of the fluid pressure gradients in the constituent materials. The approach is quite accurate and can be employed in standard finite element analysis dealing with both steady-state flow as well as coupled hydromechanical analysis [54]. The results obtained using this formulation showed that the principal directions of the hydraulic conductivity tensor closely align with those obtained from the pipe network model, while the eigenvalues remain different.

Given the computational efficiency of PNM and the accuracy of CLED in capturing complex flow behavior, it was suggested that the most pragmatic approach would be to estimate the eigenvectors of hydraulic conductivity via the PNM analysis and then assess the eigenvalues by conducting the CLED simulations only along the estimated principal directions. Such an approach was shown to provide a sufficient level of precision.

The study also explored the influence of key material properties, such as the permeability of the intact rock and the fracture aperture, on the equivalent hydraulic conductivity. The results indicated that both of these factors have a significant impact on estimations of permeability. The solution was particularly sensitive to the fracture aperture, which in turn depends on stress state, and hence, on the mechanical properties of fractured rock. Thus, in order to accurately assess the permeability of the fractured rock, it is necessary not only to estimate the in-situ aperture but also to conduct an adequate coupled analysis tracing its evolution during the deformation process.

Overall, the conducted research provided an in-depth inside into both the mechanical anisotropy of the sedimentary formations (viz. Cobourg limestone) and the hydraulic behavior of sparsely fractured crystalline rocks. The former quantified the impact of the volume fraction of argillaceous partings and their orientation on the strength and deformation properties, while the latter demonstrated the limitations of the classical models and the advantages of employing more elaborated formulations. These findings provide the basis for enhancing the modeling of mechanical and hydraulic behavior of the considered rock formations in a broad range of engineering applications.

4.2 Future Work

While the current study provided a useful insight into the modeling of mechanical anisotropy of the Cobourg limestone and the hydraulic behavior of the fractured rock masses, a number of enhancements that require further research are feasible.

One key area in this regard is to establish a broader and more explicit correlation between the fabric features and the mechanical properties of the limestone. This would entail a more accurate assessment of the volume fraction of argillaceous inclusions prior to testing, based for example on a high-resolution computed tomography (CT) scanning. The tests themselves could incorporate a wider range of confining pressures, sample orientations, and loading conditions. In that context, the linear approximations employed in this work, viz. eqs. 2.8 and 2.23, may still have to be revised to provide a more realistic representation of material characteristics.

Furthermore, the current formulation defines the anisotropy parameter as a linear function of a dyadic product of loading vectors. Again, such representation will likely to be enhanced by incorporating higher order terms in this dyadic product. Also, the range of applicability of the proposed constitutive law may be extended to incorporate the localized deformation. This can be accomplished by invoking a mechanical version of the constitutive law with embedded discontinuity, whereby the averaged strength and deformation properties in the presence of discontinuities are established through the volume averaging.

For the hydraulic analysis, the results demonstrated that the fracture connectivity plays a critical role in determining the equivalent conductivity operator. While the study explored three different modeling approaches, viz. Oda's permeability tensor, the pipe network model (PNM), and the CLED approach, further research is needed to refine these models for practical applications. In this regard, a hybrid approach suggested in this study, which involves the use of PNM to assess principal permeability directions and CLED to refine the eigenvalues, could be further validated through large-scale numerical simulations and laboratory-scale physical experiments.

The effect of stress-dependent evolution of fracture aperture on permeability is yet another topic that needs further attention. The present study reported that the equivalent hydraulic conductivity is very sensitive to the fracture aperture; the latter, however, was treated as uniform within the domain. The local aperture adjustments will occur under stress perturbations, thereby modifying permeability distribution over time. Thus, a more accurate permeability prediction can be obtained using a coupled hydro-mechanical analysis, incorporating a realistic fracture closure-dilation mechanism. Such an approach would enable the simulation of permeability evolution not only due to stress variations but also due to fluid pressure fluctuations and chemical interactions (dissolution or precipitation effects), which would greatly improve long-term hydrogeological assessments.

Finally, from a broader perspective, the findings of this study are directly applicable to underground engineering that includes tunneling, construction of deep geological repositories for waste disposal, and hydrocarbon or geothermal resource management. In this regard, the site-specific research with documented data on fracture networks could provide a platform for the validation of the methodologies proposed in this study. Environmental factors that alter permeability and anisotropy could then also be analyzed for their long-term effects on rock mass behavior.

BIBLIOGRAPHY

1. Nasseri, M. H. B., Goodfellow, S. D., Wanne, T., & Young, R. P. (2013). Thermo-hydro-mechanical properties of Cobourg limestone. *International Journal of Rock Mechanics and Mining Sciences*, *61*, 212–222.

2. Ghazvinian, E., Diederichs, M. S., Labrie, D., & Martin, C. D. (2015). An investigation on the fabric type dependency of the crack damage thresholds in brittle rocks. *Geotechnical and Geological Engineering*, *33*(6), 1409–1429.

3. Nguyen, T. S., Li, Z., Su, G., Nasseri, M. H. B., & Young, R. P. (2018). Hydro-mechanical behavior of an argillaceous limestone considered as a potential host formation for radioactive waste disposal. *Journal of Rock Mechanics and Geotechnical Engineering*, *10*(6), 1063–1081.

4. Selvadurai, A. P. S., & Najari, M. (2017). The thermo-hydro-mechanical behavior of the argillaceous Cobourg Limestone. *Journal of Geophysical Research: Solid Earth*, *122*(6), 4157–4171.

5. Béland Otis, C. (2015). *Upper Ordovician organic-rich mudstones of Southern Ontario: Drilling project results* (Open File Report 6312). Ontario Geological Survey.

6. Cavé, L., Al, T., Xiang, Y., & Vilks, P. (2009). A technique for estimating one-dimensional diffusion coefficients in low-permeability sedimentary rock using X-ray radiography: Comparison with through-diffusion measurements. *Journal of Contaminant Hydrology*, *103*(1–2), 1–12.

7. Nasseri, M. H. B., Young, R. P., Su, X., Nguyen, T. S., & Li, Z. (2018). Hydro-mechanical behaviour of the Cobourg limestone. *International Journal of Rock Mechanics and Mining Sciences, 102*, 42–51.

8. Selvadurai, A. P. S., & Niya, S. R. (2020). Effective thermal conductivity of an intact heterogeneous limestone. *Journal of Rock Mechanics and Geotechnical Engineering, 12*(4), 682–692.

9. Selvadurai, A. P. S. (2019). The Biot coefficient for a low permeability heterogeneous limestone. *Continuum Mechanics and Thermodynamics, 31*(4), 939–953.

10. Selvadurai, A. P. S. (2017). *Geomechanical characterization of the Cobourg limestone* (Technical Report NWMO-TR-2017). Nuclear Waste Management Organization.

11. Nasseri, M. H. B., & Young, R. P. (2014). *Thermo-hydro-mechanical properties of Cobourg limestone* (Technical Report NWMO-TR-2015-18). Nuclear Waste Management Organization.

12. Jaczkowski, E., Ghazvinian, E., & Diederichs, M. (2017). *Uniaxial compression and indirect tensile testing of Cobourg limestone: Influence of scale, saturation and loading rate* (Technical Report NWMO-TR-2017-17). Nuclear Waste Management Organization.

13. Perras, M. A., Paraskevopoulou, C., Hädener, P., Leith, K., Loew, S., & Amann, F. (2018). *Time dependent strength of limestone: Creep and relaxation tests* (Technical Report NWMO-TR-2018-11). Nuclear Waste Management Organization.

14. Ghazvinian, E., Perras, M. A., Langford, C., & Diederichs, M. S. (2013). A comprehensive investigation of crack damage anisotropy in Cobourg limestone and its effect on the failure envelope. *In Proceedings of GeoMontreal* (pp. 1–7). Canadian Geotechnical Society.

15. Itasca Consulting Group Inc. (2008). PFC2D/3D (Particle Flow Code in 2D/3D) Version 4.0. Itasca Consulting Group.

16. Pierce, M., Cundall, P., Potyondy, D., & Mas Ivars, D. (2007). A synthetic rock mass model for jointed rock. *In Proceedings of the 1st Canada–US Rock Mechanics Symposium* (pp. 341–349). Taylor & Francis.

17. Mas Ivars, D., Pierce, M. E., Darcel, C., et al. (2011). The synthetic rock mass approach for jointed rock mass modelling. *International Journal of Rock Mechanics and Mining Sciences, 48*(2), 219–244.

18. Farahmand, K. (2017). *Characterization of rockmass properties and excavation damage zone (EDZ) using a synthetic rock mass (SRM) approach* [Doctoral dissertation, Queen's University].

19. Vazaios, I., Farahmand, K., Vlachopoulos, N., & Diederichs, M. S. (2018). Effects of confinement on rock mass modulus: *A synthetic rock mass modelling (SRM) study. Journal of Rock Mechanics and Geotechnical Engineering, 10*(3), 436–456.

20. Diederichs, M. (2007). Mechanistic interpretation and practical application of damage and spalling prediction criteria for deep tunnelling. *Canadian Geotechnical Journal, 44*(9), 1082–1116.

21. Hajiabdolmajid, V. (2017). Modeling brittle failure of rock. In X. T. Feng (Ed.), *Rock mechanics and engineering: Volume 1* (pp. 593–621). CRC Press.

22. Moench, A. F. (1984). Double-porosity models for a fissured groundwater reservoir with fracture skin. *Water Resources Research, 20*(7), 831–846.

23. Olson, J. E., Laubach, S. E., & Lander, R. H. (2007). Combining diagenesis and mechanics to quantify fracture aperture distributions and fracture pattern permeability. *Geological Society Special Publications, 270*(1), 101–116.

24. Chen, J., & Jiang, F. (2015). Designing multi-well layout for enhanced geothermal system to better exploit hot dry rock geothermal energy. *Renewable Energy, 74*(C), 37–48.

25. Desbarats, A. J. (1987). Numerical estimation of effective permeability in sand-shale formations. *Water Resources Research, 23*(2), 273–286.

26. Jafari, A., & Babadagli, T. (2012). Estimation of equivalent fracture network permeability using fractal and statistical network properties. *Journal of Petroleum Science and Engineering, 92*, 110–123.

27. Miao, T., Yu, B., Duan, Y., & Fang, Q. (2015). A fractal analysis of permeability for fractured rocks. *International Journal of Heat and Mass Transfer, 81*, 75–80.

28. Scheidegger, A. E. (1954). Directional permeability of porous media to homogeneous fluids. *Geofisica Pura e Applicata, 28*(1), 75–90.

29. Bear, J. (1972). *Dynamics of fluids in porous media*. American Elsevier.

30. Azizmohammadi, S., & Matthäi, S. K. (2017). Is the permeability of naturally fractured rocks scale dependent? *Water Resources Research, 53*(9), 8041–8063.

31. Schulze-Makuch, D., Carlson, D. A., Cherkauer, D. S., & Malik, P. (1999). Scale dependency of hydraulic conductivity in porous media. *Ground Water, 37*(6), 904–919.

32. Martinez-Landa, L., & Carrera, J. (2005). An analysis of hydraulic conductivity scale effects in granite (Full-scale Engineered Barrier Experiment (FEBEX), Grimsel, Switzerland). *Water Resources Research, 41*(3), 1–13.

33. Min, K. B., Jing, L., & Stephansson, O. (2004). Determining the equivalent permeability tensor for fractured rock masses using a stochastic REV approach: Method and application to the field data from Sellafield, UK. *Hydrogeology Journal, 12,* 497–510.

34. Bogdanov, I. I., Mourzenko, V. V., Thovert, J. F., & Adler, P. M. (2007). Effective permeability of fractured porous media with power-law distribution of fracture sizes. *Physical Review E, 76*(3), 036309.

35. Renshaw, C. E., & Park, J. C. (1997). Effect of mechanical interactions on the scaling of fracture length and aperture. *Nature, 386*(6624), 482–484.

36. Jin, L., & Zoback, M. D. (2017). Fully coupled nonlinear fluid flow and poroelasticity in arbitrarily fractured porous media: A hybrid-dimensional computational model. *Journal of Geophysical Research: Solid Earth, 122*(10), 7626–7658.

37. Khoei, A. R., Hosseini, N., & Mohammadnejad, T. (2016). Numerical modeling of two-phase fluid flow in deformable fractured porous media using the extended finite element method and an equivalent continuum model. *Advances in Water Resources, 94*, 510–528.

38. Centeno Lobão, M., Eve, R., Owen, D. R. J., & de Souza Neto, E. A. (2010). Modelling of hydro-fracture flow in porous media. *Engineering Computations, 27*(1), 129–154.

39. Barenblatt, G. I., Zheltov, I. P., & Kochina, I. N. (1960). Basic concepts in the theory of seepage of homogeneous liquids in fissured rocks. *Applied Mathematics and Mechanics, 24*(5), 852–864.

40. Warren, J. E., & Root, P. J. (1963). The behavior of naturally fractured reservoirs. *Journal of the Society of Petroleum Engineers, 3*(3), 245–255.

41. Pruess, K., Faybishenko, B., & Bodvarsson, G. S. (1999). Alternative concepts and approaches for modeling flow and transport in thick unsaturated zones of fractured rocks. *Journal of Contaminant Hydrology, 38*(1-3), 281–322.

42. Chen, T., Clauser, C., Marquart, G., Willbrand, K., & Mottaghy, D. (2015). A new upscaling method for fractured porous media. *Advances in Water Resources, 80*, 60–68.

43. Chen, T., Clauser, C., Marquart, G., Willbrand, K., & Hiller, T. (2018). Upscaling permeability for three-dimensional fractured porous rocks with the multiple boundary method. *Hydrogeology Journal, 26*(6), 1903–1916.

44. Oda, M. (1985). Permeability tensor for discontinuous rock masses. *Géotechnique, 35*(4), 483–495.

45. Oda, M. (1986). An equivalent continuum model for coupled stress and fluid flow analysis in jointed rock masses. *Water Resources Research, 22*(13), 1845–1856.

46. Dershowitz, B., LaPointe, P., Eiben, T., & Wei, L. (2000). Integration of discrete feature network methods with conventional simulator approaches. *SPE Reservoir Evaluation & Engineering, 3*(2), 165–170.

47. Gupta, A., Penuela, G., & Avila, R. (2001). An integrated approach to the determination of permeability tensors for naturally fractured reservoirs. *Journal of Canadian Petroleum Technology, 40*(12).

48. Decroux, B., & Gosselin, O. (2013). Computation of effective dynamic properties of naturally fractured reservoirs: Comparison and validation of methods. *In EAGE Annual Conference & Exhibition Incorporating SPE Europec*. Society of Petroleum Engineers.

49. Harstad, H., Teufel, L. W., Lorenz, J. C., & Brown, S. R. (1996). *Characterization and fluid flow simulation of naturally fractured Frontier sandstone, Green River Basin, Wyoming* (SAND-96-1955). Sandia National Laboratories.

50. Priest, S. D. (1993). *Discontinuity analysis for rock engineering.* Springer.

51. Li, S. C., Xu, Z. H., & Ma, G. W. (2014). A graph-theoretic pipe network method for water flow simulation in discrete fracture networks: GPNM. *Tunnelling and Underground Space Technology, 42*, 247–263.

52. Wang, C., Wu, K., & Scott, G. (2022). Improvements to the fracture pipe network model for complex 3D discrete fracture networks. *Water Resources Research, 58*(3), e2020WR029450.

53. Ren, F., Ma, G., Wang, Y., Li, T., & Zhu, H. (2017). Unified pipe network method for simulation of water flow in fractured porous rock. *Journal of Hydrology, 547*, 80–96.

54. Jameei, A. A., & Pietruszczak, S. (2020). Embedded discontinuity approach for coupled hydromechanical analysis of fractured porous media. *International Journal for Numerical and Analytical Methods in Geomechanics*, *44*(14), 1880–1902.

55. Kanatani, K. (1985). Procedures for stereological estimation of structural anisotropy. *International Journal of Engineering Science, 23*(5), 587–598.

56. Pietruszczak, S., & Mroz, Z. (2001). On failure criteria for anisotropic cohesive-frictional materials. *International Journal for Numerical and Analytical Methods in Geomechanics, 25*(5), 509–524.

57. Moreno, R., Smedby, Ö., & Borga, M. (2011). On the efficiency of the mean intercept length tensor. *In SSBA Symposium.*

58. Selvadurai, A. P. S., & Rezaei Niya, S. M. (2020). Effective thermal conductivity of an intact heterogeneous limestone. *Journal of Rock Mechanics and Geotechnical Engineering*, *12*(4), 682–692.

59. Doube, M., Klosowski, M. M., Arganda-Carreras, I., et al. (2010). BoneJ: Free and extensible bone image analysis in ImageJ. *Bone, 47*(6), 1076–1079.

60. Harrigan, T. P., & Mann, R. W. (1984). Characterization of microstructural anisotropy in orthotropic materials using a second rank tensor. *Journal of Materials Science, 19*(3), 761–767.

61. Westin, C. F., Maier, S. E., Khidhir, B., Everett, P., Jolesz, F. A., & Kikinis, R. (1999). Image processing for diffusion tensor magnetic resonance imaging. In C. Taylor, A. Colchester, & M. Sonka (Eds.), *Medical image computing and computer-assisted intervention – MICCAI 1999* (pp. 441–452). Springer.

62. Pietruszczak, S. (2010). *Fundamentals of plasticity in geomechanics*. CRC Press.

63. Haghighat, E., & Pietruszczak, S. (2015). On the mechanical and hydraulic response of sedimentary rocks in the presence of discontinuities. *Geomechanics for Energy and the Environment, 4*, 61–72.

64. Rudnicki, J. W., & Rice, J. R. (1975). Conditions for the localization of deformation in pressure-sensitive dilatant materials. *Journal of the Mechanics and Physics of Solids, 23*(6), 371–394.

65. Zimmerman, R. W., & Yeo, I. W. (2000). Fluid flow in rock fractures: From the Navier-Stokes equations to the cubic law. *Geophysical Monograph - American Geophysical Union, 122*, 213–224.

66. Zhang, J., Liu, R., Yu, L., Li, S., Wang, X., & Liu, D. (2022). An equivalent pipe network modeling approach for characterizing fluid flow through three-dimensional fracture networks: Verification and applications. *Water, 14*(10), 1582.

67. Pietruszczak, S., & Mroz, Z. (1981). Finite element analysis of deformation of strain-softening materials. *International Journal for Numerical Methods in Engineering*, *17*(3), 327–334.

68. Pietruszczak, S. (1993). On homogeneous and localized deformation in water-infiltrated soils. *Journal of Damage Mechanics*, *8*(3), 233–253.

69. Jameei, A. A., & Pietruszczak, S. (2021). On hydromechanical interaction during propagation of localized damage in rocks. *Minerals, 11*(2), 1–12.

70. Chen, S. H., Feng, X. M., & Isam, S. (2008). Numerical estimation of REV and permeability tensor for fractured rock masses by composite element method. *International Journal for Numerical and Analytical Methods in Geomechanics, 32*(12), 1459–1477.